Formation-Flying Planar Periodic Orbits in the Presence of Intersatellite Lorentz Force

CHAO PENG
YANG GAO
Chinese Academy of Sciences
Beijing, China.

This study presents formation-flying periodic orbits in a new satellite-relative motion scenario, which considers the presence of intersatellite Lorentz force. A nonlinear dynamical model for the proposed relative motion is established based on the Hill–Clohessy–Wiltshire equation, under the assumption that a chief satellite generates a rotating magnetic dipole while a constantly charging deputy satellite moves close to the artificial magnetic field of the chief satellite. Moreover, we assume that the barycenter of the proposed system is constrained in a circular reference orbit, and the rotating magnetic axis of the dipole is perpendicular to the reference orbital plane. We first derived equilibrium points (and analyzed their stabilities), an integral constant, and zero-velocity surfaces for the proposed relative motion based on system parameters, such as the charge-to-mass ratio of the deputy satellite, the moment and rotating rate of the magnetic dipole, and the angular velocity of the reference orbit. With regard to the zero-velocity surfaces, bounded periodic orbits in the reference orbital plane are searched out using Poincare maps. Planar periodic orbits near the equilibrium points are numerically computed via differential correction based on the stability characteristic of equilibrium points, and a special case is analytically solved using the Lindstedt−Poincare method. The periodic orbits of relative motion presented in this study differ from those in traditional satellite formation flying. The difference suggests potential applications of the presented periodic orbits, such as propellantless satellite formation maintenance and noncontact capture of electrostatically charged space debris.

I. INTRODUCTION

An electrically charged particle moving in a magnetic field experiences Lorentz force, which is one of the fundamental physical principles in electrodynamics. If the electric charge of the particle is q and its velocity relative to a magnetic field $\mathbf{B}$ is $\mathbf{v}_r$, then the Lorentz force acting on the charged particle is computed as $\mathbf{F}_L = q\mathbf{v}_r \times \mathbf{B}$. With a logical rationale, if a charged satellite moves in the geomagnetic field, then it experiences Lorentz force that can possibly be a propellantless means to change and control satellite orbits. This orbital control scheme was proposed by Peck [1], and the orbits of charged satellites were called "Lorentz-augmented orbits."

Lorentz-augmented orbits are analogous to the motion of charged dust grains in planetary magnetic fields [2], and the motion of a charged ballistic missile is affected by Lorentz-force perturbations when it crosses the ionosphere[3]. Similarly, the motion of electrically charged Earth-orbit artificial satellites, which is induced by the geomagnetic field, is also perturbed by Lorentz force [4], [5]. The SCATHA satellite, which was launched in 1979, conducted an experiment on active charge control by emitting electrons or ions to study the phenomenon of satellite surface charging [6]. Thereafter, the Cluster satellite also successfully implemented an active charge control by emitting indium ions [7]. Although the primary purpose of the active charge control for both the SCATHA and Cluster satellites is to alleviate charging accumulation to decrease induced radiation effects, the practical adjustment of satellite surface charging in space supports the potential utilization of Lorentz force in orbit control.

The capability of Lorentz force to control the orbit of a satellite remains limited to a certain degree and Lorentz-augmented orbits are still in their conceptual research stage; nevertheless this innovative idea has attracted the attention of numerous scholars and a number of applications of Lorentz-augmented orbits have been proposed from the perspective of orbital dynamics. Streetman *et al.* [8] proposed new Lorentz-augmented synchronous orbits; developed Lorentz control schemes to change semimajor axis, eccentricity, and inclination using a bang-bang type control strategy [9]; and examined the effects of Lorentz-augmented orbits on Jovian gravity-assist maneuvers [10], [11]. Pollock *et al.* presented inclination change and responsive coverage for Earth observation using Lorentz force [12], [13], derived Lagrange's planetary equations for the motion of electrostatically charged satellite, and proposed the conditions for Lorentz-augmented planetary escape from equatorial and inclined orbits [14]. These types of Lorentz-augmented orbits typically require high charging levels, which are technically challenging. To date, the possibility of implementing the charging level in the aforementioned orbital control schemes remains uncertainty and poses numerous technical challenges even in the future. This uncertainty has motivated us to find feasible schemes to utilize Lorentz force. One attempt has shifted our attention to relative orbit control for

satellite formation flying, which requires significantly lower charging levels because changing relative motion is considerably easier than changing the satellite orbit relative to Earth.

Research on the orbital dynamics of satellite formation flying mainly covers relative motion modeling, formation design, formation reconfiguration, and formation maintenance. Control strategies that use electromagnetic force or electrostatic force have been proposed recently for formation flying. In one approach that applies electromagnetic force, satellites in a formation are made to produce artificial magnetic fields. The interaction among magnetic fields could control the relative motion of satellite. Kong *et al.* proposed a satellite formation control scheme called electromagnetic formation flight (EMFF) [15]. Umair *et al.* conducted a research on the dynamics and control of EMFF in deep space [16] and studied formation reconfiguration and maintenance in low Earth orbit for EMFF [17]. King *et al.* proposed another approach that applies electromagnetic force [18], i.e., controlling satellite relative motion using intersatellite electrostatic force (Coulomb force). Schaub focused on formation maintenance using Coulomb force [19] and proposed one-dimensional (1D) constrained Coulomb structure control with charge saturation [20]. Felicetti *et al.* evaluated the control strategies for maintaining spacecraft formation [21]. Similarly, the Lorentz force induced by the magnetic field of the Earth can be used to control satellite formation given that a charged satellite moves in a low Earth orbit [22]. Pollock *et al.* analyzed relative motion in a circular orbit using Lorentz force, which is beneficial for designing rendezvous and fly-around maneuvers [23]. Peng and Gao recently proposed Lorentz-force-perturbed orbits for establishing J_2-invariant formation [24] and a bang-bang Lorentz force control for reconfiguring formation in a near-circular reference orbit [25]. Ludwik and Christopher designed an optimal control strategy that combined continuous Lorentz force actuation with impulsive thrusting for reconfiguring formation [26].

In this study, we introduce a new space relative motion scenario, in which intersatellite Lorentz force provides a new means to control satellite formation. We focus on identifying periodic relative orbits in this relative motion scenario, which is possibly the first step in understanding this new dynamical system. On the basis of the concept of EMFF, we first assume that the chief satellite is equipped with high-temperature superconducting wires and is capable of generating an artificial magnetic field that can be simplified as a rotating magnetic dipole. In addition, a charged deputy satellite is moving close to the artificial magnetic field of the chief satellite. Both the chief satellite and the deputy satellite are subjected to intersatellite Lorentz force. Moreover, the reference orbit is considered a high-altitude circular orbit, such as a geosynchronous orbit, where charging the satellite is easier than in a low Earth orbit because of the low-density plasma environment. The Lorentz force exerted on the charged deputy satellite by the Earth or the planetary magnetic field is disregarded. We established

the equations for relative motion in the presence of intersatellite Lorentz force based on the preceding basic assumptions, and then derived equilibrium points (and analyzed their stabilities), an integral constant, and zero-velocity surfaces for the new dynamical system. Two categories of planar periodic orbits are presented. The first category is bounded on the reference orbital plane, whereas the second is bounded around the equilibrium points. The former is found using Poincare maps, which is inspired by bounded orbits with regard to zero-velocity surfaces, whereas the latter, with a special case analytically solved using the Lindstedt–Poincare method, are numerically computed via differential correction, which is an analogue of the Lyapunov orbits [27] in the restricted circular three-body dynamics. Several simplifications are made for this research as follows.

1) The relative motion is planar and the axis of the dipole is perpendicular to the reference orbital plane.
2) Only one class of equilibrium points is considered when the deputy satellite is negatively charged.
3) The barycenter of the chief satellite and the deputy satellite moves in a Keplerian circular reference orbit.

Despite these simplifications, the dynamics of the proposed system still provide new insights into periodic relative motion that considers the intersatellite Lorentz force.

Evidently, how to build up desired charge and a rotating magnetic dipole in space, especially a large amount of charge and magnetic strength, is still under research. They are technically challenging and no feasible solutions are presented in detail in this paper. The relevant technologies have been proposed in existing literature, for example, [28] indicates that a satellite has a charging level on the order of 10^{-6} C/kg is feasible, and [29] shows that the magnetic dipole moment of 0.1 T $\cdot$ m^3 can be produced. These representative quantities are used to analyze the relative motion and periodic orbits described in the following sections. Our attention is mainly focused on system dynamics, which aims to present conceptual research on formation flying considering intersatellite Lorentz force. It helps us better understand the amount of charge and magnetic strength that are required to implement some unique formations closely related to Lorentz force. It is worthy to note that the deputy satellite could be a damaged one or debris such that any destructive effect resulted from charging is not necessary to consider.

The rest of this paper is organized as follows. Relative motion that considers the intersatellite Lorentz force is modeled in Section II. Section III presents the equilibrium points, integral constant, and zero-velocity surfaces in the proposed dynamical system. Section IV describes the bounded planar periodic orbits using Poincare maps, whereas Section V describes the planar periodic orbits near the equilibrium points. The conclusions of the study and potential applications are provided in Section VI.
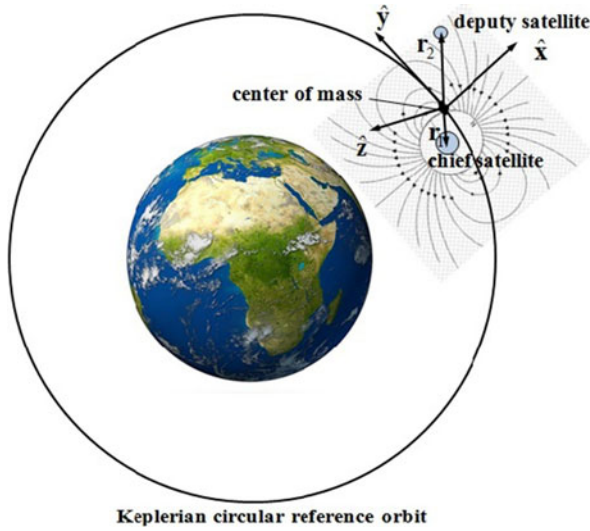
Fig. 1. Relative motion that considers the intersatellite Lorentz force in the LVLH coordinates.

II. MODELING RELATIVE MOTION IN THE PRESENCE OF INTERSATELLITE LORENTZ FORCE

A relative motion scenario with two satellites (see Fig. 1), commonly referred to as the chief satellite and the deputy satellite, is considered. Both satellites are subjected to gravitational force and Lorentz force. The equation for the relative motion with the barycenter (center of mass) of the chief satellite and the deputy satellite in a circular reference orbit can be derived using the well-known Hill–Clohessy–Wiltshire equation as follows [30]:

$$\begin{cases} \ddot{x}_1 - 2n\dot{y}_1 - 3n^2x_1 = f_{Lx_1} \\ \quad \ddot{y}_1 + 2n\dot{x}_1 = f_{Ly_1} \\ \quad \ddot{z}_1 + n^2z_1 = f_{Lz_1} \end{cases} \tag{1}$$

$$\begin{cases} \ddot{x}_2 - 2n\dot{y}_2 - 3n^2x_2 = f_{Lx_2} \\ \quad \ddot{y}_2 + 2n\dot{x}_2 = f_{Ly_2} \\ \quad \ddot{z}_2 + n^2z_2 = f_{Lz_2} \end{cases} \tag{2}$$

where n is the mean orbital rate of the circular reference orbit; $\mathbf{r}_1 = [x_1\,y_1\,z_1]^{\mathrm{T}}$ and $\mathbf{r}_2 = [x_2\,y_2\,z_2]^{\mathrm{T}}$ are position vectors of the chief satellite and the deputy satellite in local-vertical-local-horizontal (LVLH) coordinates; and $[f_{Lx_1}\,f_{Ly_1}\,f_{Lz_1}]^{\mathrm{T}}$ and $[f_{Lx_2}\,f_{Ly_2}\,f_{Lz_2}]^{\mathrm{T}}$ are the three components of the Lorentz-force acceleration acting on the chief satellite and the deputy satellite, respectively. The LVLH coordinate frame originates from the barycenter. The unit vectors of the axes of the LVLH coordinate $[\hat{\mathbf{x}}\,\hat{\mathbf{y}}\,\hat{\mathbf{z}}]$ are also depicted in Fig. 1, where $\hat{\mathbf{x}}$ is in the direction of the orbital radius vector, $\hat{\mathbf{z}}$ is in the direction of the orbital momentum vector, and $\hat{\mathbf{y}}$ completes the right-handed orthogonal LVLH coordinates. Notably, these motion equations are valid only when the reference orbit is circular and the relative orbit coordinates ($x_1\,y_1\,z_1\,x_2\,y_2\,z_2$) are considerably smaller than the reference orbital radius.

If the chief satellite and the deputy satellite are affected only by the attracting force of Earth's gravity, i.e.,

$[f_{Lx_1}\,f_{Ly_1}\,f_{Lz_1}]^{\mathrm{T}}$ and $[f_{Lx_2}\,f_{Ly_2}\,f_{Lz_2}]^{\mathrm{T}}$ are all set to zero, then the resulting differential equations, namely, (1) and (2) can be analytically integrated to find closed-form solutions for relative motion [30]. If the expressions for $[f_{Lx_1}\,f_{Ly_1}\,f_{Lz_1}]^{\mathrm{T}}$ and $[f_{Lx_2}\,f_{Ly_2}\,f_{Lz_2}]^{\mathrm{T}}$ are complicated nonlinear functions, then finding an analytical solution for (1) and (2) is generally difficult, and numerical integration is necessary to determine spacecraft relative orbit at a desired time instant. In this study, (1) and (2), which are modeled via intersatellite Lorentz force, eventually form a complex dynamical system.

The derivation of a potential function associated with the electromagnetic field is required to model Lorentz force acceleration using Lagrange mechanics, which is defined as [31]

$$U_{\mathrm{EM}} = -q\mathbf{v_r} \cdot \mathbf{A} \tag{3}$$

where q is the charged amount of the deputy satellite, and $\mathbf{v}_r$ is the velocity of the charged deputy satellite relative to the rotating magnetic field of the chief satellite, which is computed as follow:

$$\mathbf{v_r} = \dot{\mathbf{r}} - \boldsymbol{\omega}_c \times \mathbf{r} \tag{4}$$

where $\mathbf{r} = [x\,y\,z]^{\mathrm{T}} = [x_2-x_1\;y_2-y_1\;z_2-z_1]^{\mathrm{T}}$ and $\dot{\mathbf{r}} = [\dot{x}\,\dot{y}\,\dot{z}]^{\mathrm{T}} = [\dot{x}_2-\dot{x}_1\;\dot{y}_2-\dot{y}_1\;\dot{z}_2-\dot{z}_1]^{\mathrm{T}}$ are the position and velocity vectors of the deputy satellite relative to the chief satellite, respectively; and $\boldsymbol{\omega}_c$ is the angular velocity vector of the magnetic rotation observed in the LVLH coordinates. The vector potential $\mathbf{A}$ for the magnetic dipole is defined as [31]

$$\begin{aligned} \mathbf{A} &= \frac{B_0}{r^2}(\hat{\mathbf{N}} \times \hat{\mathbf{r}}) \\ &= \frac{B_0}{r^3}\left[(z\hat{N}_y - y\hat{N}_z)\;\;(x\hat{N}_z - z\hat{N}_x)\;\;(y\hat{N}_x - x\hat{N}_y)\right]^{\mathrm{T}} \end{aligned} \tag{5}$$

where $\hat{\mathbf{r}} = [\hat{r}_x\,\hat{r}_y\,\hat{r}_z] = [(x/r)\,(y/r)\,(z/r)]$ is the unit vector of the relative position of the deputy satellite with respect to the chief satellite, $r = \sqrt{x^2 + y^2 + z^2}$ is the distance between the deputy satellite and the chief satellite, B_0 is the magnetic dipole moment, and $\hat{\mathbf{N}} = [N_x\,N_y\,N_z]^{\mathrm{T}}$ is the dipole direction unit vector. Moreover, the magnetic dipole is assumed to be rotating around the dipole direction unit vector as follows:

$$\boldsymbol{\omega}_c = \omega_c[N_x\,N_y\,N_z]^{\mathrm{T}}. \tag{6}$$

The Lagrange function of the proposed dynamical system is then formulated by considering that the two spacecrafts (the chief satellite and the deputy satellite) experience intersatellite Lorentz force in a magnetic dipole field [32]

$$\begin{aligned} L^{(0)} &= m_1\mathcal{L}_1^{(0)} + m_2\mathcal{L}_2^{(0)} - U_{\mathrm{EM}} \\ &= m_1\mathcal{L}_1^{(0)} + m_2\mathcal{L}_2^{(0)} + q\mathbf{v_r} \cdot \mathbf{A} \end{aligned} \tag{7}$$

where m_1 and m_2 are the masses of the chief satellite and the deputy satellite, respectively; and $\mathcal{L}_k^{(0)}$ is presented as

follow:

$$\mathcal{L}_k^{(0)} = \frac{1}{2}(\dot{x}_k^2 + \dot{y}_k^2 + \dot{z}_k^2) + n(x_k\dot{y}_k - y_k\dot{x}_k + a\dot{y}_k)$$
$$+ \frac{3}{2}n^2a^2 + \frac{3}{2}n^2x_k^2 - \frac{n^2}{2}z_k^2 \qquad (8)$$

where subscripts $k = 1, 2$ denote the chief satellite and the deputy satellite, respectively; and a is the semimajor axis of the circular reference orbit.

Equations (1) and (2) are derived from Euler–Lagrange equation $d(\partial L/\partial \dot{\mathbf{r}}_1)/dt - \partial L/\partial \mathbf{r}_1 = 0$ and $d(\partial L/\partial \dot{\mathbf{r}}_2)/dt - \partial L/\partial \mathbf{r}_2 = 0$, where the Lorentz-force acceleration components are

$$\begin{cases} f_{Lx_2} = \dfrac{q}{m_2}\dfrac{B_0}{r^3}\{3(\hat{N} \cdot \hat{r})(\dot{y}\hat{r}_z - \dot{z}\hat{r}_y) + \dot{z}\hat{N}_y - \dot{y}\hat{N}_z \\ \qquad -\omega_c(x\hat{N}_z - z\hat{N}_x)[3(\hat{N} \cdot \hat{r})\hat{r}_z - \hat{N}_z] \\ \qquad +\omega_c(y\hat{N}_x - x\hat{N}_y)[3(\hat{N} \cdot \hat{r})\hat{r}_y - \hat{N}_y]\} \\[2mm] f_{Ly_2} = \dfrac{q}{m_2}\dfrac{B_0}{r^3}\{3(\hat{N} \cdot \hat{r})(\dot{z}\hat{r}_x - \dot{x}\hat{r}_z) + \dot{x}\hat{N}_z - \dot{z}\hat{N}_x \\ \qquad -\omega_c(y\hat{N}_x - x\hat{N}_y)[3(\hat{N} \cdot \hat{r})\hat{r}_x - \hat{N}_x] \quad (9) \\ \qquad +\omega_c(z\hat{N}_y - y\hat{N}_z)[3(\hat{N} \cdot \hat{r})\hat{r}_z - \hat{N}_z]\} \\[2mm] f_{Lz_2} = \dfrac{q}{m_2}\dfrac{B_0}{r^3}\{3(\hat{N} \cdot \hat{r})(\dot{x}\hat{r}_y - \dot{y}\hat{r}_x) + \dot{y}\hat{N}_x - \dot{x}\hat{N}_y \\ \qquad -\omega_c(z\hat{N}_y - y\hat{N}_z)[3(\hat{N} \cdot \hat{r})\hat{r}_y - \hat{N}_y] \\ \qquad +\omega_c(x\hat{N}_z - z\hat{N}_x)[3(\hat{N} \cdot \hat{r})\hat{r}_x - \hat{N}_x]\} \end{cases}$$

$$f_{Lx_1} = -\frac{m_2}{m_1}f_{Lx_2}, \quad f_{Ly_1} = -\frac{m_2}{m_1}f_{Ly_2}, \quad f_{Lz_1} = -\frac{m_2}{m_1}f_{Lz_2}. \qquad (10)$$

When (2) is subtracted from (1), the equation for the relative motion is derived as follows:

$$\begin{cases} \ddot{x} - 2n\dot{y} - 3n^2x = f_{Lx} \\ \ddot{y} + 2n\dot{x} = f_{Ly} \quad (11) \\ \ddot{z} + n^2z = f_{Lz} \end{cases}$$

where $[f_{Lx}\ f_{Ly}\ f_{Lz}]^T = [f_{Lx_2}\ f_{Ly_2}\ f_{Lz_2}]^T - [f_{Lx_1}\ f_{Ly_1}\ f_{Lz_1}]^T$, which is expressed as

$$f_{Lx} = (1+\epsilon)f_{Lx_2}, \quad f_{Ly} = (1+\epsilon)f_{Ly_2}, \quad f_{Lz} = (1+\epsilon)f_{Lz_2} \qquad (12)$$

where $\epsilon = m_2/m_1$. In addition, a parameter (q/m) $(m = m_2)$, which is called the charge-to-mass ratio, is proposed.

When (12) is substituted into (11), the equations for relative motion that considers the presence of intersatellite Lorentz force are derived. The functions of Lorentz-force acceleration are evidently complicated and finding an analytical solution for (11) is difficult. The axis of the dipole is assumed to be perpendicular to the reference orbit plane, i.e., $\hat{N} = [0\ 0\ \pm 1]^T$. When $\hat{N} = [0\ 0\ 1]^T$ is substituted into

Eq. (12), the Lorentz-force acceleration values are given by

$$\begin{cases} f_{Lx} = (1+\epsilon)\dfrac{q}{m} \\ \quad B_0\dfrac{[(-x^2 - y^2 + 2z^2)\dot{y} - 3yz\dot{z} + \omega_c x(x^2 + y^2 - 2z^2)]}{r^5} \\[2mm] f_{Ly} = (1+\epsilon)\dfrac{q}{m} \\ \quad B_0\dfrac{[(x^2 + y^2 - 2z^2)\dot{x} + 3xz\dot{z} + \omega_c y(x^2 + y^2 - 2z^2)]}{r^5} \\[2mm] f_{Lz} = (1+\epsilon)\dfrac{q}{m}B_0\dfrac{3z[y\dot{x} - x\dot{y} + \omega_c(x^2 + y^2)]}{r^5}. \end{cases}$$
$$(13)$$

If $\hat{N} = [0\ 0\ -1]^T$, then the Lorentz-force acceleration values are

$$\begin{cases} f_{Lx} = -(1+\epsilon)\dfrac{q}{m} \\ \quad B_0\dfrac{[(-x^2 - y^2 + 2z^2)\dot{y} - 3yz\dot{z} - \omega_c x(x^2 + y^2 - 2z^2)]}{r^5} \\[2mm] f_{Ly} = -(1+\epsilon)\dfrac{q}{m} \\ \quad B_0\dfrac{[(x^2 + y^2 - 2z^2)\dot{x} + 3xz\dot{z} - \omega_c y(x^2 + y^2 - 2z^2)]}{r^5} \\[2mm] f_{Lz} = -(1+\epsilon)\dfrac{q}{m}B_0\dfrac{3z[y\dot{x} - x\dot{y} - \omega_c(x^2 + y^2)]}{r^5}. \end{cases}$$
$$(14)$$

In (13) and (14), the parameters (q/m) and ω_c can be positive or negative. If these two parameters in (14) are contrary to those in (13), then no difference exists between (13) and (14). Therefore, only the case in Eq. will be analyzed in this study. Although the proposed dynamical system is highly nonlinear and the general analytical solutions cannot be easily found, special solutions may be discovered using dynamical systems theory.

III. EQUILIBRIUM POINTS, INTEGRAL CONSTANT, AND ZERO-VELOCITY SURFACES

A. Locations and Stabilities of the Equilibrium Points

The equations for relative motion, i.e., (11), can be considerably simplified using dimensionless variables. Let $\zeta = tn$ be the new time variable. The time rate of a state variable is written as

$$\frac{d\mathbf{x}}{dt} = \frac{d\mathbf{x}}{d\zeta}\frac{d\zeta}{dt} = \mathbf{x}'n \qquad (15)$$

where the notation $(\ )' = d(\ )/d\zeta$, which represents the dimensionless time rate, is introduced. The equations for relative motion, i.e., (11) and (13), are derived by defining the dimensionless unit of the range variable α $(\alpha^3 = (1+\epsilon) \cdot |(q/m)B_0\omega_c/3n^2|)$ and setting $[X\ Y\ Z]^T = [x\ y\ z]^T/\alpha$, as

follows:

$$\begin{cases} X'' - 2Y' - 3X = \pm 3\big[\beta Y'(-X^2 - Y^2 + 2Z^2) - 3\beta Y ZZ' \\ \qquad\qquad + X(X^2 + Y^2 - 2Z^2)\big]/R^5 \\ Y'' + 2X' = \pm 3\big[\beta X'(X^2 + Y^2 - 2Z^2) + 3\beta X ZZ' \\ \qquad\qquad + Y(X^2 + Y^2 - 2Z^2)\big]/R^5 \\ Z'' + Z = \pm 9Z\big[\beta Y X' - \beta X Y' + (X^2 + Y^2)\big]/R^5 \end{cases}$$
(16)

where $\beta = n/\omega_c$ and $R = \sqrt{X^2 + Y^2 + Z^2}$. The signs at the right sides of the equations are negative when $(q/m) < 0$ and positive when $(q/m) > 0$. In addition, the dimensionless forms of (1) and (2) are derived as follow with respect to (16):

$$\begin{cases} X_1'' - 2Y_1' - 3X_1 = \dfrac{-\epsilon}{1+\epsilon}\big(X'' - 2Y' - 3X\big) \\ Y_1'' + 2X_1' = \dfrac{-\epsilon}{1+\epsilon}\big(Y'' + 2X'\big) \\ Z_1'' + Z_1 = \dfrac{-\epsilon}{1+\epsilon}\big(Z'' + Z\big) \end{cases}$$
(17)

$$\begin{cases} X_2'' - 2Y_2' - 3X_2 = \dfrac{1}{1+\epsilon}\big(X'' - 2Y' - 3X\big) \\ Y_2'' + 2X_2' = \dfrac{1}{1+\epsilon}\big(Y'' + 2X'\big) \\ Z_2'' + Z_2 = \dfrac{1}{1+\epsilon}\big(Z'' + Z\big) \end{cases}$$
(18)

The dimensionless position vector of the barycenter in the LVLH coordinates are represented by $\mathbf{R}_c = [X_c \ Y_c \ Z_c]^T$, and computed as

$$\begin{cases} X_c = (X_1 + \epsilon X_2)/(1 + \epsilon) \\ Y_c = (Y_1 + \epsilon Y_2)/(1 + \epsilon) \\ Z_c = (Z_1 + \epsilon Z_2)/(1 + \epsilon). \end{cases}$$
(19)

The dynamics of the motion of the barycenter is derived using (17) and (18) as follows:

$$\begin{cases} X_c'' - 2Y_c' - 3X_c = 0 \\ Y_c'' + 2X_c' = 0 \\ Z_c'' + Z_c = 0. \end{cases}$$
(20)

The barycenter should be located at the origin of the LVLH coordinates as depicted in Fig 1, i.e., $X_c = Y_c = Z_c = X_c' = Y_c' = Z_c' = 0$, which is the trivial solution for (20). From (17)–(19), the trivial solution results in the following conditions:

$$[X_1 \ Y_1 \ Z_1 \ X_1' \ Y_1' \ Z_1']^T = \frac{-\epsilon}{1+\epsilon}[X \ Y \ Z \ X' \ Y' \ Z']^T \quad (21)$$

$$[X_2 \ Y_2 \ Z_2 \ X_2' \ Y_2' \ Z_2']^T = \frac{1}{1+\epsilon}[X \ Y \ Z \ X' \ Y' \ Z']^T \quad (22)$$

where $\epsilon = m_2/m_1$ is defined in (12). If the initial orbital states of the chief satellite and the deputy satellite satisfy (21) and (22), then the barycenter will always remain at the origin of the LVLH coordinates. In this case, once the relative motion modeled by (16) is solved, the motion of the chief satellite and the deputy satellite can be readily obtained with respect to (17) and (18). Therefore, this study focuses only on (16). The expression of relative motion equations in vector form, as presented in (23) and (24), is frequently beneficial, and is easy to conduct using the dimensionless variable $\mathbf{X} = [X \ Y \ Z \ X' \ Y' \ Z']^T$

$$\mathbf{X}' = \boldsymbol{f}(\mathbf{X}) \tag{23}$$

where Eqn. (24) is shown at the bottom of the page.

The locations of the equilibrium points $\mathbf{X}_e$ ($\mathbf{X}_e = [X_e \ Y_e \ Z_e \ 0 \ 0 \ 0]^T$) for this dynamical system can be de-

$$\boldsymbol{f}(\mathbf{X}) = [\,f_1 \ f_2 \ f_3 \ f_4 \ f_5 \ f_6\,]^T = \begin{bmatrix} X' \\ Y' \\ Z' \\ 3X + 2Y' \pm 3\dfrac{[\beta Y'(-X^2 - Y^2 + 2Z^2) - 3\beta Y ZZ' + X(X^2 + Y^2 - 2Z^2)]}{R^5} \\ -2X' \pm 3\dfrac{[\beta X'(X^2 + Y^2 - 2Z^2) + 3\beta X ZZ' + Y(X^2 + Y^2 - 2Z^2)]}{R^5} \\ -Z \pm 3\dfrac{3Z[\beta Y X' - \beta X Y' + (X^2 + Y^2)]}{R^5} \end{bmatrix}$$
(24)

termined by setting $X' = Y' = Z' = 0$ and $f(\mathbf{X}) = 0$

$$X_e = \pm 1, \quad Y_e = 0, \quad Z_e = 0,$$
$$\text{if } (q/m) < 0; \quad (25)$$
$$X_e = 0, \quad Y_e^2 = 2Z_e^2, \quad Z_e = \pm(2/\sqrt{3})^{1/3},$$
$$\text{if } (q/m) > 0; \quad (26)$$
$$X_e = \pm(1/4\sqrt{6})^{1/3}, \quad Y_e = 0, \quad Z_e^2 = 5X_e^2,$$
$$\text{if } (q/m) > 0. \quad (27)$$

The system has three types of equilibrium points. If $(q/m) < 0$, then the points are located on the X-axis and the distance from the origin to the equilibrium points is one dimensionless unit. If $(q/m) > 0$, i.e., (26) and (27), then two types of equilibrium points are located on the YZ or XZ plane. This study focuses only on the first case depicted in (25). When $(q/m) > 0$, the other two cases can be analyzed in the same manner.

From dynamical systems theory, the stability of the equilibrium points can be determined by linearizing the dynamical equations at these points. Let $\delta\mathbf{X} = \mathbf{X} - \mathbf{X}_e$, where $\mathbf{X}_e$ denotes the equilibrium points. The linearization regarding any of these points is as follow:

$$\delta\mathbf{X}' = D_{\mathbf{X}_e}f \cdot \delta\mathbf{X} \quad (28)$$

where $D_{\mathbf{X}_e}f$ is the derivative of f evaluated at equilibrium point $\mathbf{X}_e$. The terms of the differential $D_{\mathbf{X}_e}f$ have been computed, and the results are shown in Appendix A. $D_{\mathbf{X}_e}f$, which governs the linear flow near the equilibrium points $\mathbf{X}_e = [\pm 1\ 0\ 0\ 0\ 0\ 0]^T$ (see (25)), is explicitly written as follow:

$$D_{\mathbf{X}_e}f = \begin{bmatrix} 0 & 0 & 0 & 1 & 0 & 0 \\ 0 & 0 & 0 & 0 & 1 & 0 \\ 0 & 0 & 0 & 0 & 0 & 1 \\ 9 & 0 & 0 & 0 & 2+3\beta & 0 \\ 0 & -3 & 0 & -2-3\beta & 0 & 0 \\ 0 & 0 & -10 & 0 & 0 & 0 \end{bmatrix}$$
$$(29)$$

The eigenvectors and eigenvalues of $D_{\mathbf{X}_e}f$ should be found to determine the stability of the linear system. λ is an eigenvalue if and only if

$$\det(D_{\mathbf{X}_e}f - \lambda\mathbf{I}) = 0. \quad (30)$$

A series of trivial calculations leads to the following characteristic equation:

$$\lambda^6 + (9\beta^2 + 12\beta + 8)\lambda^4 + (90\beta^2 + 120\beta - 47)\lambda^2 - 270 = 0. \quad (31)$$

When the substitution of $\tau = \lambda^2$ is performed, (31) is reduced to

$$\tau^3 + (9\beta^2 + 12\beta + 8)\tau^2 + (90\beta^2 + 120\beta - 47)\tau - 270 = 0. \quad (32)$$

The resulting third-order polynomial can be explicitly solved and the roots are computed as

$$\tau_1 = -10 \quad (33)$$
$$\tau_2 = \frac{1}{2}(2 - 12\beta - 9\beta^2$$
$$+ \sqrt{112 - 48\beta + 108\beta^2 + 216\beta^3 + 81\beta^4}) \quad (34)$$
$$\tau_3 = \frac{1}{2}(2 - 12\beta - 9\beta^2$$
$$- \sqrt{112 - 48\beta + 108\beta^2 + 216\beta^3 + 81\beta^4}). \quad (35)$$

The following expression is easy to find:

$$|2 - 12\beta - 9\beta^2| < \sqrt{112 - 48\beta + 108\beta^2 + 216\beta^3 + 81\beta^4}. \quad (36)$$

Therefore, finding that

$$\tau_2 > 0 \quad \tau_3 < 0 \quad (37)$$

is also easy.

The six eigenvalues are $\lambda_{k_{1,2}} = \pm\sqrt{\tau_k}$, where $k = 1, 2, 3$. Consider the following pair:

$$\lambda_{2_{1,2}} = \pm\sqrt{\tau_2}. \quad (38)$$

where $\lambda_{2_{1,2}}$ are real because $\tau_2 > 0$, with one positive value and one negative value, the corresponding eigenmodes have an exponentially decaying and growing term. The resulting solution, which is the "center × center × saddle" behavior, indicates that an unstable motion occurs near the equilibrium point. In the same manner, the other two types of equilibrium points in (26) and (27) are determined to be both unstable.

B. Integral Constant and Zero-velocity Surfaces

In Section II, Lorentz force $\mathbf{f}_L$ was derived using a potential function associated with the electromagnetic field, which was defined as $U_{EM} = -q\mathbf{v}_r \cdot \mathbf{A}$[31]. Moreover, the terms $-3X$ and Z on the left side of (16) are the gradients of $-3X^2/2$ and $Z^2/2$, respectively. The terms $[-2Y'\ 2X']$, which are obtained from the translation of the coordinate systems between the inertial coordinates and the LVLH coordinates, will not affect the total energy of the system. Therefore, the dynamical system in (16) must have an integral constant, which can be derived by starting with a scalar combination of the dynamical variables $X'X' + Y'Y' + Z'Z'$

$$X'X' + Y'Y' + Z'Z''$$
$$= X' \cdot f_4 + Y' \cdot f_5 + Z' \cdot f_6$$
$$= 3XX' - ZZ' \pm 3[XX'(X^2 + Y^2 - 2Z^2)$$
$$+ YY'(X^2 + Y^2 - 2Z^2) + 3ZZ'(X^2 + Y^2)]/R^5$$
$$= D_t\left(\frac{3}{2}X^2 - \frac{1}{2}Z^2 \mp 3\frac{X^2 + Y^2}{R^3}\right) \quad (39)$$

where D_t is the derivative of the term in the bracket with respect to time, and $(f_4\ f_5\ f_6)$ are expressed in (24).

Evidently

$$D_t\left(\frac{X'^2 + Y'^2 + Z'^2}{2}\right) = X'X'' + Y'Y'' + Z'Z'' \quad (40)$$

and

$$D_t\left(\frac{X'^2 + Y'^2 + Z'^2}{2}\right) = D_t\left(\frac{3}{2}X^2 - \frac{1}{2}Z^2 \mp 3\frac{X^2 + Y^2}{R^3}\right) \quad (41)$$

Then

$$\frac{1}{2}(X'^2 + Y'^2 + Z'^2) = \left(\frac{3}{2}X^2 - \frac{1}{2}Z^2 \mp 3\frac{X^2 + Y^2}{R^3}\right) - \frac{1}{2}C \quad (42)$$

where C is a constant. Thereafter, the following case is derived:

$$\left(3X^2 - Z^2 \mp 6\frac{X^2 + Y^2}{R^3}\right) - (X'^2 + Y'^2 + Z'^2) = C. \quad (43)$$

This constant or conserved quantity is called the "energy integral." It is referred as the "energy" or "energy integral" in this study because it is a conserved quantity.

If the velocity is set to zero at a given energy level, then a set of system states is determined and obtained by implicitly solving the following equation:

$$3X^2 - Z^2 \mp 6\frac{X^2 + Y^2}{R^3} = C. \quad (44)$$

The solution set for this equation is a 2-D surface that may provide considerable information about the possible dynamics at a given energy level. When the deputy satellite arrives at the zero-velocity surface, its velocity relative to the chief satellite is zero, and thus, it cannot pass through the surface. Therefore, the zero-velocity surface restricts possible dynamics by showing which regions in space are unreachable at a given energy level.

The signs on the left side of (43) and (44) depend on the sign of (q/m). In the remainder of this paper, only the case of $(q/m) < 0$ is considered with the assumption that space debris or a satellite can always be negatively charged because debris is generally easier to be negatively charged than positively charged. The forms of (43) and (44) are transformed into

$$3X^2 - Z^2 + 6\frac{X^2 + Y^2}{R^3} - (X'^2 + Y'^2 + Z'^2) = C \quad (45)$$

$$3X^2 - Z^2 + 6\frac{X^2 + Y^2}{R^3} = C. \quad (46)$$

The value of the energy integral at the equilibrium point is

$$C_{(\pm1,0,0)} = 9 \quad (47)$$

where subscript $(\pm1, 0, 0)$ represents the position coordinates of the equilibrium point. The zero-velocity surfaces and their projection on the XY-plane for energy levels of $1.1C_{(\pm1,0,0)}$, $C_{(\pm1,0,0)}$, and $0.9C_{(\pm1,0,0)}$ are shown in Figs. 2–4.

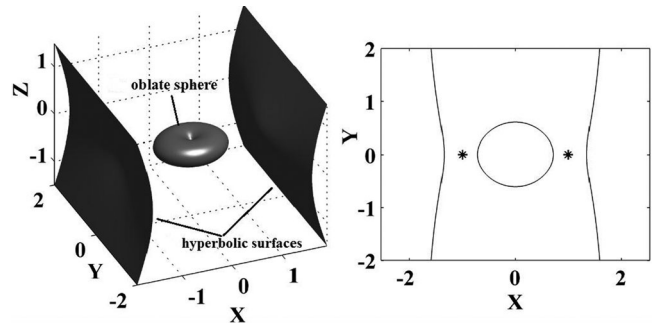As shown in the Figs. 2–4, the chief satellite always remains at the origin of the frame. Under the assumptions

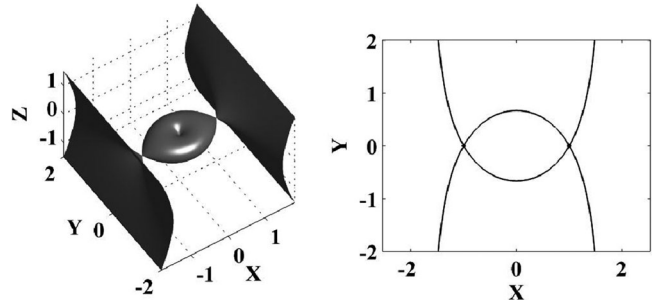Fig. 2. Zero-velocity surfaces and the projection at $1.1C_{(\pm1,0,0)}$.

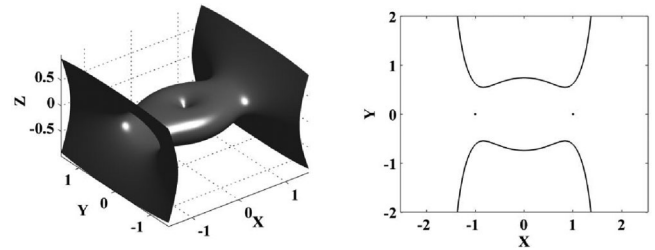Fig. 3. Zero-velocity surfaces and the projection at $C_{(\pm1,0,0)}$.

Fig. 4. Zero-velocity surfaces and the projection at $0.9C_{(\pm1,0,0)}$.

that the deputy satellite can establish or modify the amount of charging in the order of 10^{-6} C/kg [28], the magnetic dipole moment $B_0 = 0.1$ T·m^3 [29], the angular velocity $\omega_c = 1$ rad/s, parameter $\epsilon = m_2/m_1 = 1$, and the reference orbit is geostationary orbit, the range between the chief satellite and the equilibrium point is approximately 2.3 m.

At an energy level of $1.1C_{(\pm1,0,0)}$ (see Fig. 2), the allowable orbits are separated into two disconnected domains. At this energy level, the chief satellite and the deputy satellite contained in an oblate sphere (see Fig. 2). The deputy satellite orbiting the chief satellite never goes beyond the boundary of the oblate sphere (i.e., relative motion is bounded). If the deputy satellite is far from the chief satellite, then the orbits in space with unbounded hyperbolic surfaces (see Fig. 2) as the boundary cannot arrive in the oblate sphere. Fig. 3 indicates that the barrier between the chief satellite and external space just opens at an energy level of $C_{(\pm1,0,0)}$. However, the two domains on each side of the equilibrium points are still disconnected and no orbit can pass through. In Fig. 4, the barrier between chief satellite and external space is removed when the energy level is further reduced, and a "neck" occurs near the

equilibrium point, which indicates that the deputy satellite can possibly escape from the vicinity of the chief satellite. Notably, escape is only possible through the small neck.

C. Two Types of Planar Periodic Orbits

The remainder of this paper mainly focuses on planar relative motion, which will provide substantial conclusions regarding periodic relative motion that considers the intersatellite Lorentz force. To model planar relative motion ($Z = \dot{Z} = 0$), (16) (($q/m) < 0$) is reduced to its planar form as follows:

$$\begin{cases} X'' - 2Y' - 3X = -3\dfrac{-\beta Y' + X}{R^3} \\ Y'' + 2X' = -3\dfrac{\beta X' + Y}{R^3} \end{cases} \quad (48)$$

where $R = \sqrt{X^2 + Y^2}$.

The equilibrium points are

$$X = \pm 1, \quad Y = 0. \quad (49)$$

They exhibit the classical "center × saddle" behavior based on the linearization analysis. Similarly, (48) has an energy integral, as follows:

$$3X^2 + \frac{6}{\sqrt{X^2 + Y^2}} - (X'^2 + Y'^2) = C. \quad (50)$$

The energy integral value at the equilibrium point is $C_{(\pm 1,0)} = 9$, and the zero-velocity curves (ZVC) are solved via

$$3X^2 + \frac{6}{\sqrt{X^2 + Y^2}} = C. \quad (51)$$

Consider the following initial position and velocity with energy integral values of $1.1C_{(\pm 1,0)}$, $C_{(\pm 1,0)}$, and $0.9C_{(\pm 1,0)}$.

$$[X_0 \ Y_0 \ X_0' \ Y_0']^T = [0.5 \ 0 \ 0 \ 1.6882]^T \quad (52)$$
$$[X_0 \ Y_0 \ X_0' \ Y_0']^T = [-0.8 \ 0 \ 0 \ 0.6481]^T \quad (53)$$
$$[X_0 \ Y_0 \ X_0' \ Y_0']^T = [-0.6 \ 0 \ 0 \ 1.7263]^T. \quad (54)$$

The corresponding relative orbit shown in Fig. 5(a) is obtained by integrating the fundamental equation of motion, i.e., (48), into the initial condition in (52) for 100 time units. The relative orbit corresponds to an energy integral of $1.1C_{(\pm 1,0)}$, thereby limiting the motion of the deputy satellite in the oblate sphere around the chief satellite. Moreover, if the initial condition is set using (53) (subjected to an energy level of $C_{(\pm 1,0)}$), then the corresponding orbit remains in the oblate sphere around the chief satellite, as shown in Fig. 5(b). Finally, the initial condition in (54) with an energy level of $0.9C_{(\pm 1,0)}$ is considered. As shown in Fig. 5(c), the deputy satellite orbits the chief satellite approximately 20 time units before reaching outside space. It arrives at the ZVC several times before leaving the chief satellite through the neck.

Finding two types of planar periodic orbits is easy. First, the ZVC indicate the existence of bounded motion, as illustrated in Fig. 5(a) and (b). The numerical simulation shows that Lorentz force can maintain bounded relative
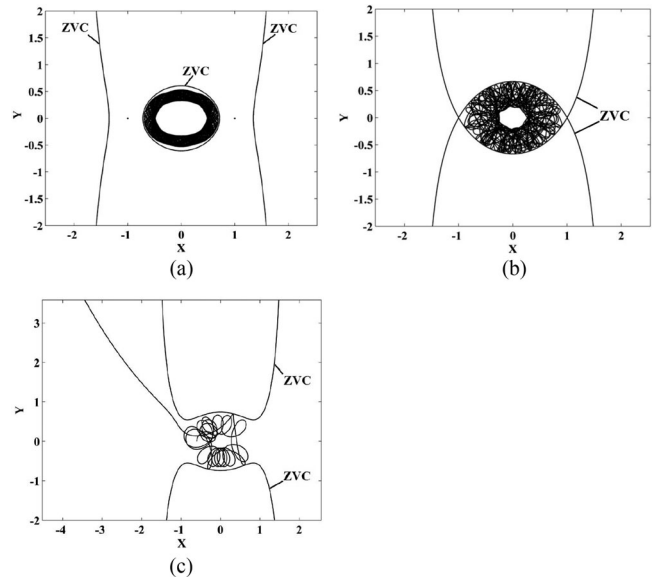

Fig. 5. Orbit around the chief satellite with energy integral values of $1.1C_{(\pm 1,0)}$, $C_{(\pm 1,0)}$, and $0.9C_{(\pm 1,0)}$.

orbits when energy integral C is appropriately selected ($C \geq C_{(\pm 1,0)}$). Because the charge-to-mass ratio (q/m), the magnetic dipole moment B_0 and the angular velocity ω_c, which determine the value of parameter α (see Section III-A), can be arbitrarily set, the desired value of C can be set to generate bounded relative orbits. This speculation is derived from the fact that the bounded periodic motion of the deputy satellite relative to the chief satellite may be possible.

In addition, periodic motion may occur near the equilibrium point because this point exhibits a "center × saddle" behavior, which is inspired by the existence of Lyapunov orbits near the collinear Lagrange points in the circular restricted three-body dynamics. The presence of the center manifold near the equilibrium point can assist in finding periodic orbits.

Therefore, two types of periodic orbits are first analyzed in this study: bounded periodic orbits with respect to the ZVC and periodic orbits around the equilibrium points. In the first step of this study, the planar cases of periodic orbits, which are described in Sections IV and V, are investigated.

IV. SEARCHING OUT PLANAR STABLE PERIODIC ORBITS USING POINCARE MAPS

In dynamical systems theory or celestial mechanics, a Poincare map, which is typically interpreted as a discrete-time dynamical system, provides a fundamental tool for analyzing orbital flows. The dimension of the original continuous-time dynamical system is reduced by at least one order with a judicious choice of Poincare maps. Poincare maps can provide a considerably larger global picture of the dynamics of a system than linear analysis.

Consider a system of differential equations $\dot{\mathbf{x}} = \mathbf{F}(\mathbf{x})$, and a point $\mathbf{x}^*$. Let $\boldsymbol{\phi}(\mathbf{x}^*, t)$ be the point of the trajectory $\boldsymbol{\chi}(\mathbf{x}^*, [0 \ t_f])$ at time t ($0 < t < t_f$), where $\boldsymbol{\chi}(\mathbf{x}^*, [0 \ t_f])$ is

the trajectory curve obtained by flowing $\mathbf{x}^*$ forward by time t_f in the system $\dot{\mathbf{x}} = \mathbf{F}(\mathbf{x})$. In addition, let a hyperplane Σ be through $\mathbf{x}^*$ and traverse to the flow, i.e., all trajectories starting from Σ flow through it and are not parallel to it. Assume that $\boldsymbol{\phi}(\mathbf{x}^*, \tau^*)$ is again in Σ for some $\tau^* > 0$. It also assume that no other intersections of $\boldsymbol{\phi}(\mathbf{x}^*, t)$ with Σ near $\mathbf{x}^*$ exist. For $\mathbf{x}$ near $\mathbf{x}^*$, there is a nearby time $\tau(\mathbf{x})$ such that $\boldsymbol{\phi}(\mathbf{x}, \tau(\mathbf{x}))$ is in Σ. Then, $\mathbf{P}(\mathbf{x}) = \boldsymbol{\phi}(\mathbf{x}, \tau(\mathbf{x}))$ is the Poincare map.

With regard to the orbital flow of a periodic orbit, its intersection on the Poincare map always remains at the same position, which is frequently called a fixed point of a discrete-time dynamical system. Meanwhile, other types of flow, such as quasi-periodic or chaotic orbits, can also be identified using a Poincare map, thereby providing significant insight into the orbit structure of a dynamical system. In this study, Poincare maps are used to search for planar periodic orbits in the reference orbital plane. The phase space of the planar system for the proposed relative motion is 4-D and is difficult to visualize. It is not only convenient but also quite natural to restrict the energy integral to a particular value in which case a 3-D continuous-time dynamical system is obtained. Furthermore, a Poincare map with a fixed energy integral provides a 2-D discrete-time dynamical system, which is used to identify periodic orbits.

A. Poincare Map With an Energy Integral of $C = 1.1C_{(\pm1,0)}$

First, Poincare maps for planar systems are created with an energy integral of $C = 1.1C_{(\pm1,0)}$. We select four different β values for the system in (48): $-0.001, -0.1, 0.01$, and 1. A total of 300 initial conditions along the X-axis, whose velocity magnitude is determined based on an energy integral of $C = 1.1C_{(\pm1,0)}$ are chosen. The equations of motion, i.e., (48), are numerically integrated into 2000 time units with the proposed initial conditions. The data points are searched for the crossings of the XZ-plane with a positive Y-axis velocity ($Y' > 0$). A point is considered located on the XZ-plane when $|Y| < 10^{-6}$. The X and $\dot{X}$ (or V_x) coordinates of the points on the XZ-plane are recorded and used to create Poincare maps, which are shown in Fig. 6.

As shown in Fig. 6(a), a fixed point ($X = 0.3786$ and $X' = 0$) exists. Subsequently, the entire initial states can be recovered because the energy integral is prescribed at $C = 1.1C_{(\pm1,0)}$. The magnitude of the velocity is determined by the energy integral ($|V| = 2.5254$) and the Poincare map is defined for the crossings with $\dot{Y} > 0$; thus, the complete initial condition is derived as follows:

$$[X_0 \ Y_0 \ X_0' \ Y_0']^{\mathrm{T}} = [0.3786 \ 0 \ 0 \ 2.5254]^{\mathrm{T}}. \quad (55)$$

The corresponding orbit is obtained as shown in Fig. 7 by numerically integrating (48) into the aforementioned initial condition that was forwarded for 40 time units. It is a periodic orbit that exists around the chief satellite in the rotating LVLH frame. The gray line in the figure (the closed curve outside) denotes the ZVC with an energy integral of $C = 1.1C_{(\pm1,0)}$. The figure shows that the deputy satellite
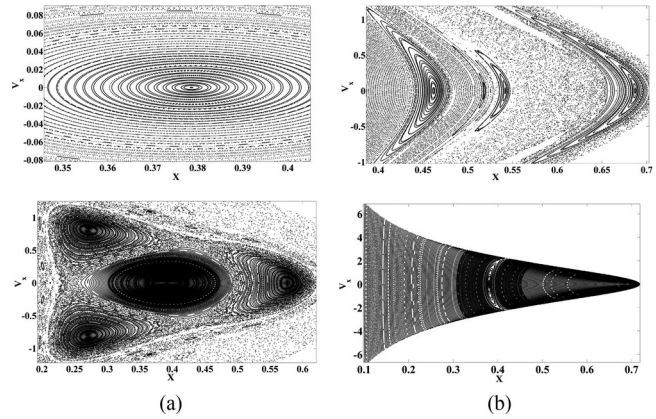

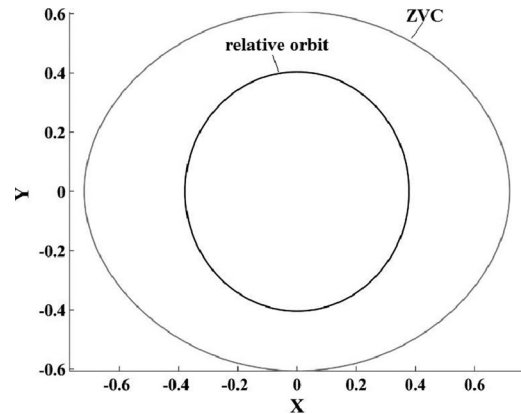Fig. 6. Poincare maps with $C = 1.1C_{(\pm1,0)}$ and $\beta = -0.001, -0.1, 0.01.1$.

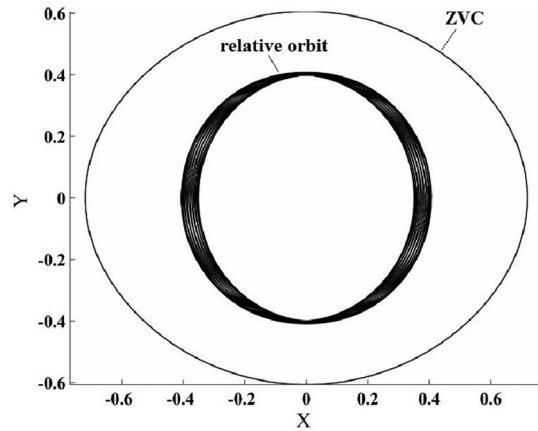Fig. 7. Orbit generated by the fixed point in Fig. 6(a).

Fig. 8. Orbit generated by the point near the fixed point in Fig. 6(a).

does not deviate from the periodic orbit, which strongly suggests that the periodic orbit is stable.

In addition, the circles near the fixed point of the Poincare map in Fig. 6(a) suggest that quasi-periodic orbits exist. For example, the initial condition, which is far from the fixed point but well within the map, is selected to be

$$[X_0 \ Y_0 \ X_0' \ Y_0']^{\mathrm{T}} = [0.35 \ 0 \ 0 \ 2.7587]^{\mathrm{T}}. \quad (56)$$

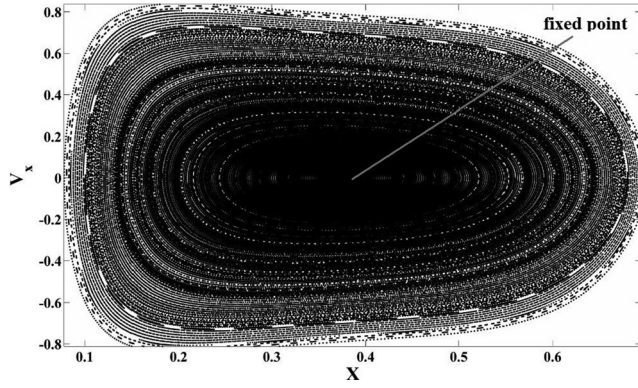This initial condition leads to the orbit shown in Fig. 8. The quasi-periodic relative orbit remains bounded.

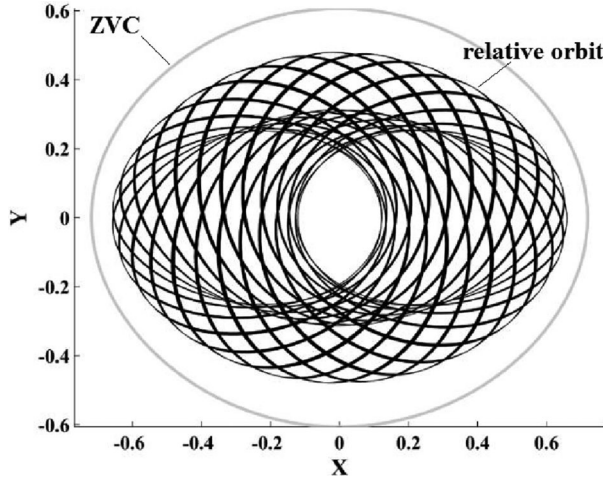Fig. 9. Global picture of the Poincare map with $C = 1.1C_{(\pm1,0)}$ and $\beta = -0.001$.

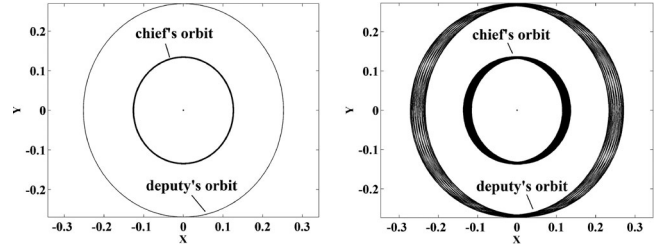Fig. 10. Orbit generated by the point far away from the fixed point.

Fig. 11. Orbits of the chief satellite and the deputy satellite that correspond to the relative motions in Figs. (7) and (8).
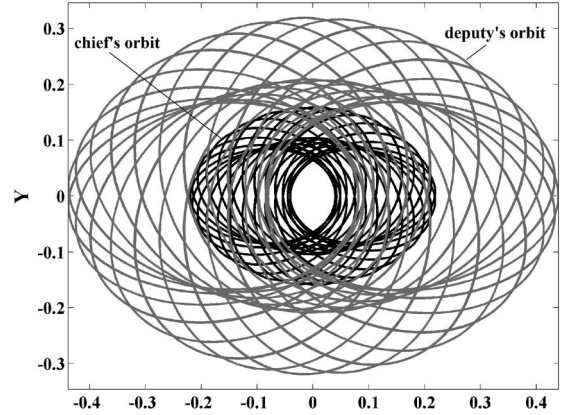

Fig. 12. Orbits of the chief satellite and the deputy satellite that correspond to the relative motion in Fig. 10.

Furthermore, observe the global picture of the dynamics of the system shown in Fig. 9, which is under the condition of $C = 1.1C_{(\pm1,0)}$ and $\beta = -0.001$. In the figure, numerous closed curves travel around the only fixed point in the Poincare map. From the principles of Poincare maps, a conclusion can be drawn that the orbits within this ZVC are all quasi-periodic except for one periodic orbit generated by the fixed point.

The condition of $X_0 = 0.2$ and $X_0' = 0.6$, which is sufficiently far from the fixed point ($X_0 = 0.3786$, $X_0' = 0$), is presented as an example. The complete initial condition computed at $C = 1.1C_{(\pm1,0)}$ is

$$[X_0 \ Y_0 \ X_0' \ Y_0']^{\mathrm{T}} = [0.2 \ 0 \ 0.6 \ 4.4565]^{\mathrm{T}}. \quad (57)$$

The orbit starting from the initial state in (57) is illustrated in Fig. 10. The figure indicates that the area occupied by the orbit is considerably larger than that shown in Fig. 8.

Let $\epsilon = m_2/m_1 = 1/2$, and $[X_0 \ Y_0 \ X_0' \ Y_0']^{\mathrm{T}}$ are set by (55) and (56) without considering the motion in the Z-axis. The motions of the chief satellite and the deputy satellite are obtained as shown in Fig. 11 by numerically integrating (17) and (18) with the initial conditions in (21) and (22).

The origin shown in Fig. 11 is the barycenter. The left subplot corresponds to the relative motion in Fig. 7, whereas the right subplot corresponds to that in Fig. 8. As shown in Fig. 7, if the relative motion is a periodic orbit, then the motions of the chief satellite and the deputy satellite are also periodic orbits. By contrast, if the relative motion is a quasi-periodic orbit, then the motion of the chief satellite and the deputy satellite are also quasi-periodic orbits. Similarly, the orbits of the chief satellite and the deputy satellite that correspond to the relative motions shown in Fig. 10 are depicted in Fig. 12.

Consider the other three Poincare maps in Fig. 6(b)–(d), which are analyzed using the same method. As indicated in the Poincare map with $\beta = -0.1$, four fixed points exist, all with $X' = 0$. The four sets of fixed points correspond to the following four sets of states

$$[X_0 \ Y_0 \ X_0' \ Y_0']_a^{\mathrm{T}} = [0.4619 \ 0 \ 0 \ 1.9313]^{\mathrm{T}} \quad (58)$$
$$[X_0 \ Y_0 \ X_0' \ Y_0']_b^{\mathrm{T}} = [0.5187 \ 0 \ 0 \ 1.5731]^{\mathrm{T}} \quad (59)$$
$$[X_0 \ Y_0 \ X_0' \ Y_0']_c^{\mathrm{T}} = [0.5419 \ 0 \ 0 \ 1.4329]^{\mathrm{T}} \quad (60)$$
$$[X_0 \ Y_0 \ X_0' \ Y_0']_d^{\mathrm{T}} = [0.6874 \ 0 \ 0 \ 0.4961]^{\mathrm{T}}. \quad (61)$$

Four types of periodic orbits are obtained by integrating (48) with the initial conditions in (58)–(61) for 40 time units, as shown in Fig. 13. With the exception of the last orbit shown in Fig. 13(d), all the other periodic orbits move around the chief satellite and have different extreme points in the radial direction. Moreover, the motions of the chief satellite and the deputy satellite that correspond to the four periodic orbits are shown in Fig. 14.

In Fig. 6(b), several closed curves also encircle the fixed points, and the orbits generated by the curves near the fixed
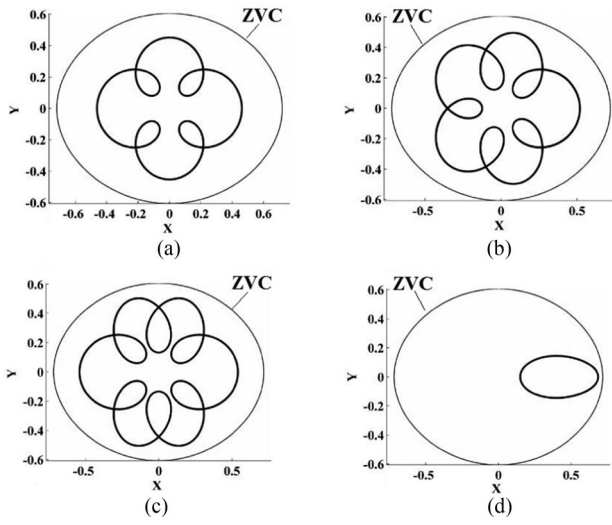
Fig. 13. Four types of periodic orbits generated by the four sets of fixed points in Fig. 6(b).
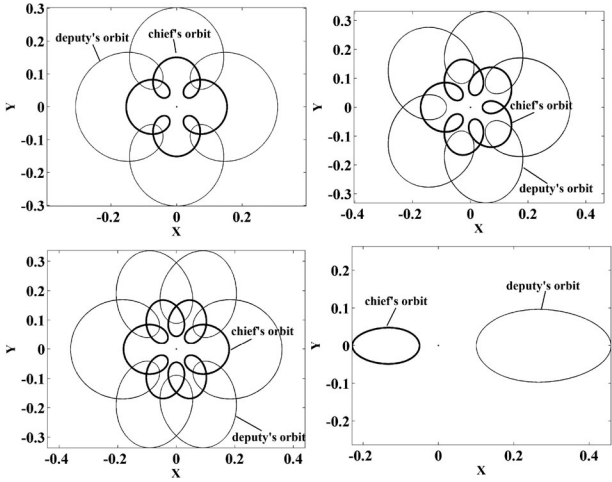

Fig. 14. Orbits of the chief satellite and the deputy satellite that correspond to the relative motions in Fig. 13.
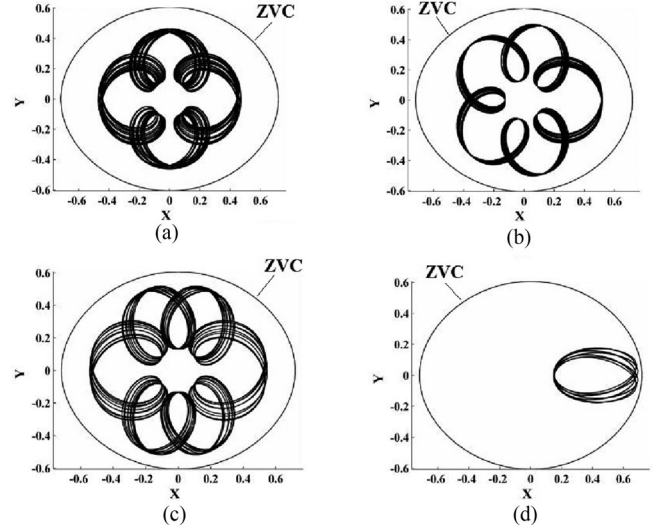

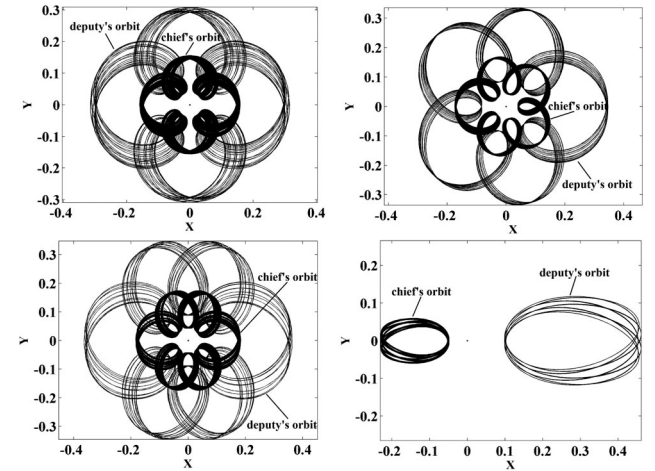Fig. 15. Quasi-periodic orbits generated by the points near the fixed points in Fig. 6(b).

Fig. 16. Orbits of the chief satellite and the deputy satellite that correspond to the relative motions in Fig. 15.
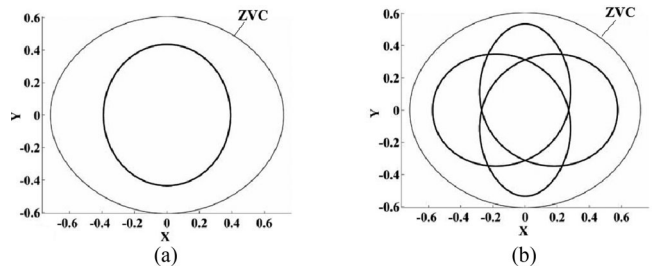

Fig. 17. Two types of periodic orbit when $\beta = 0.01$.

points are quasi-periodic orbits. The shapes of the quasi-periodic orbits are similar to that of the periodic orbits generated by the fixed points, namely, quasi-periodic orbits that are oscillating near the periodic orbit. The following four sets of initial conditions are established to obtain the four types of quasi-periodic orbits presented in Fig. 15

$$[X_0 \ Y_0 \ X'_0 \ Y'_0]_a^{\mathrm{T}} = [0.45 \ 0 \ 0 \ 2.0102]^{\mathrm{T}} \quad (62)$$

$$[X_0 \ Y_0 \ X'_0 \ Y'_0]_b^{\mathrm{T}} = [0.52 \ 0 \ 0 \ 1.5651]^{\mathrm{T}} \quad (63)$$

$$[X_0 \ Y_0 \ X'_0 \ Y'_0]_c^{\mathrm{T}} = [0.537 \ 0 \ 0 \ 1.4623]^{\mathrm{T}} \quad (64)$$

$$[X_0 \ Y_0 \ X'_0 \ Y'_0]_d^{\mathrm{T}} = [0.68 \ 0 \ 0 \ 0.5574]^{\mathrm{T}}. \quad (65)$$

Similarly, the orbits of the chief satellite and the deputy satellite, which are all quasi-periodic, are depicted in Fig. 16. As shown in Figs. 11, 14, and 16, it is easy to determine that the shape of the orbits of the deputy satellite is similar to that of the relative orbits and that the shapes of the orbits of the chief satellite and the relative orbits are symmetric with respect to the barycenter. For simplicity,

the orbits of the chief satellite and the deputy satellite will not be discussed in the following simulation cases.

When $\beta = 0.01$ or $\beta = 1$, the Poincare maps have four or two fixed points, respectively, as shown in Fig. 6(c) and (d). Two types of orbits generated by the two points on the X-axis in Fig. 6(c) are shown in Fig. 17. The two periodic orbits when $\beta = 1$ are shared in Fig. 18. As shown
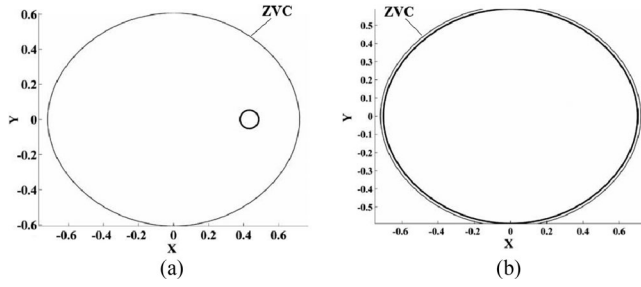
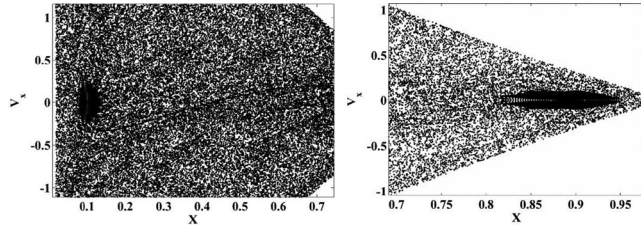Fig. 18.   Two types of periodic orbit when $\beta = 1$.

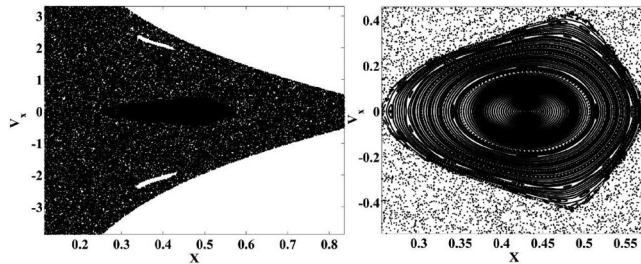Fig. 19.   Poincare maps ($C = C_{(\pm 1,0)}$, $\beta = -0.001$).

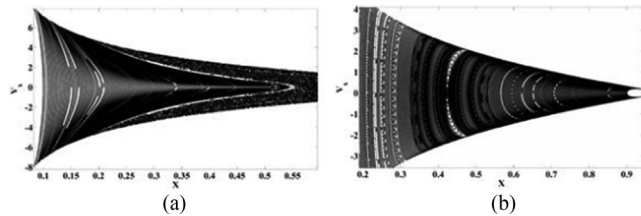Fig. 20.   Poincare maps ($C = C_{(\pm 1,0)}$, $\beta = 0.01$).

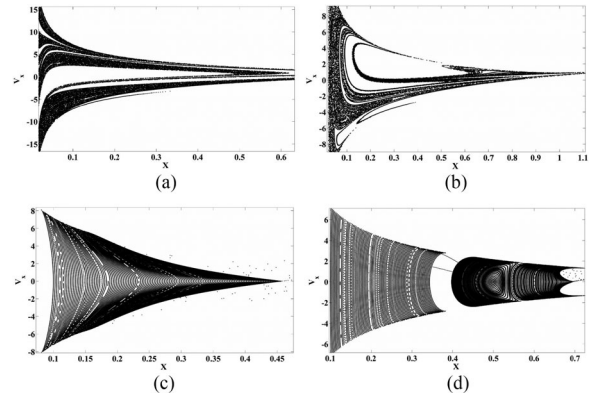Fig. 21.   Poincare maps ($C = C_{(\pm 1,0)}$, $\beta = -0.1, 1$).

Fig. 22.   Poincare maps ($C = 0.9C_{(\pm 1,0)}$, $\beta = -0.001, 0.01, -0.1, 1$).

points surrounded by a few closed curves exist. The area of the closed curves is relatively small and most of the region in the map is full of discrete points. This condition indicates that periodic and quasi-periodic orbits exist; however most orbits generated by the discrete points in Fig. 19 are chaotic and unpredictable. If $\beta = 0.01$, then the chaotic property can also be observed in the Poincare map shown in Fig. 20.

When the absolute value of β is sufficiently large, the number of discrete points decreases and the curves surround the fixed points. As shown in Fig. 21(a), when $\beta = -0.1$, the left part of the section is full of curves, whereas the right part is full of discrete points. Therefore, the chaotic characteristic in the system is weaker than those in Figs. 19−20. When $\beta = 1$, the chaotic characteristic nearly disappears because few discrete points are shown in Fig. 21(b).

For the situation in which the energy constant C is smaller than $C_{(\pm 1,0)}$, let $C = 0.9C_{(\pm 1,0)}$. The four Poincare maps for different levels of β are created (see Fig. 22). When $\beta = -0.001$ or $\beta = 0.01$, no fixed point exists in the maps shown in Fig 22(a) and (b), which suggests that all the orbits generated in these cases are not periodical.

When $\beta = -0.1$ and $\beta = 1$, the Poincare maps are depicted in Fig. 22(c) and (d), respectively. These figures show that the Poincare maps are mainly constituted by curves and a few scattered discrete points; hence, the orbits in the two cases are nearly periodic and quasi-periodic.

In this section, a few bounded periodic orbits in the reference orbital plane are searched out using Poincare maps. These periodic orbits, which differ from those in traditional satellite formation flying, demonstrate potential application in spacecraft formation. For example, a space station can maintain a number of small service satellites using propellantless Lorentz force because certain periodic orbits steadily run around the chief satellite. Moreover, the stable periodic orbits that do not travel around the chief satellite [see Figs. 13(d) and 18(a)] indicate that the deputy satellite can remain static with respect to the chief satellite.

in Figs. 17 and 18, three orbits surround the chief satellite (the origin), whereas one orbit does not [see Fig. 18(a)].

In this section, the Poincare maps with an energy integral of $C = 1.1C_{(\pm 1,0)}$ are examined. The periodic and quasi-periodic orbits are verified via numerical simulation under different values of β. However, discovering numerous discrete points in Fig. 6 is easy. These discrete points represent the extensive classes of chaotic orbits that are not analyzed in detail. These periodic and quasi-periodic orbits can be applied to a new concept of satellite formation that is entirely different from traditional ones.

B. Poincare Map With Energy Integrals of $C = C_{(\pm 1,0)}$ and $C = 0.9C_{(\pm 1,0)}$

Poincare maps with an energy integral of $C = C_{(\pm 1,0)}$ are provided in Figs. 19−21. When $\beta = -0.001$, two fixed

V. COMPUTING PLANAR PERIODIC ORBITS NEAR THE EQUILIBRIUM POINTS

In this section, periodic orbits near the equilibrium points are computed using the classical differential

correction method by taking advantages of the symmetry of motion equations. In addition, analytic solutions for a special case of these periodic orbits are obtained by using the Lindstedt–Poincare method.

A. Symmetry in the Dynamical System and Symmetric Orbits

When (48) is considered, $f(\mathbf{X})$ in (23) is expressed as

$$f(\mathbf{X}) = \begin{bmatrix} f_1 \\ f_2 \\ f_3 \\ f_4 \end{bmatrix} = \begin{bmatrix} X' \\ Y' \\ 3X + 2Y' - 3\frac{-\beta Y' + X}{R^3} \\ -2X' - 3\frac{\beta X' + Y}{R^3} \end{bmatrix} \quad (66)$$

where

$$\mathbf{X} = [X\ Y\ X'\ Y']^{\mathrm{T}}. \quad (67)$$

The symmetry in the system can be deduced through the following theorem.

Theorem: Let $\mathbf{X}_0 = [X_0\ Y_0\ X_0'\ Y_0']^{\mathrm{T}} \in \mathbf{R}^4$ be a point in the phase space of the system in (23) and (66), and let $\chi(\mathbf{X}_0, [0\ T])$ be the trajectory curve obtained by flowing $\mathbf{X}_0$ forward in time T. In addition, let $\phi(\mathbf{X}_0, t)$ be the point of the trajectory $\chi(\mathbf{X}_0, [0\ T])$ at time t. Set $\mathbf{X}_f = \phi(\mathbf{X}_0, T)$, then

$$\chi^*(\mathbf{AX}_f, [0\ T]) \equiv \mathbf{A} \cdot \chi(\mathbf{X}_f, [0\ -T]) \quad (68)$$

solves the system with $\phi^*(\mathbf{AX}_f, 0) = \mathbf{AX}_f$ and $\phi^*(\mathbf{AX}_f, T) = \mathbf{AX}_0$, where

$$\mathbf{A} = \begin{bmatrix} 1 & 0 & 0 & 0 \\ 0 & -1 & 0 & 0 \\ 0 & 0 & -1 & 0 \\ 0 & 0 & 0 & 1 \end{bmatrix} \quad (69)$$

The theorem states that if trajectory χ takes $\mathbf{X}_0$ to $\mathbf{X}_f$ in time T along path C in the phase space, then trajectory χ^* takes $\mathbf{AX}_0$ to $\mathbf{AX}_f$ at the same time along path $C^*(C^* = \mathbf{A}C)$, which is only a reflection of C across the XZ-plane with a time reversal along C. The theorem is similar to the circular restricted three-body problem [33] and its proof is not provided in this paper.

The theorem is beneficial for computing planar periodic orbits. Suppose that at time $t = 0$, a trajectory χ begins at a point $\mathbf{X}_0$ on the X-axis with a velocity normal to the XZ-plane, i.e., it only has velocity in the Y-axis direction. If trajectory χ returns to the XZ-plane at a later time $t = \tau$ with a velocity in the opposite direction of its initial velocity, then the orbit is T-periodic with $T = 2\tau$ and we obtain $\mathbf{AX}_0 = \mathbf{X}_0$ and $\mathbf{AX}_f = \mathbf{X}_f$, where $\mathbf{X}_f = \phi(\mathbf{X}_0, \tau)$. Hence

$$\phi(\mathbf{X}_0, 2\tau) = \phi^*(\mathbf{X}_f, \tau) = \mathbf{X}_0. \quad (70)$$

This trajectory can be computed using the Newton differential correction procedure. In such procedure, the parameters X_0, Y_0' and τ can vary to satisfy the terminal condition as

$$Y(\tau) = X'(\tau) = 0. \quad (71)$$

B. Computation of Symmetric Periodic Orbits Via Differential Correction

The linearized model (see (28)) indicates that the equilibrium points exhibits "center × saddle" behavior. However, the linear model is insufficient for conducting accurate studies on the dynamics near the equilibrium points. Therefore, numerical solutions that take advantage of the symmetry of the problem and the differential correction method (Newton iterations) are necessary.

Let $\mathbf{X}_0 = [X_0\ Y_0\ X_0'\ Y_0']^{\mathrm{T}}$ be the system states in the dynamics $\mathbf{X}' = f(\mathbf{X})$ (see (66)). Coordinate X_0 is held fixed to find the initial conditions for the periodic orbit. Let $Y_0 = X_0' = 0$ and search for Y' and τ to satisfy the following constraint equation:

$$\varphi(Y', \tau) = [Y(\tau)\ X'(\tau)]^{\mathrm{T}} = [0\ 0]^{\mathrm{T}}. \quad (72)$$

A Newton iteration for this problem is

$$x_{n+1} = x_n - [D\varphi(x_n)]^{-1}\varphi(x_n) \quad (73)$$

with $x = [Y', \tau]^{\mathrm{T}}$ and $x_0 = [Y_0', \tau_0]^{\mathrm{T}}$. In this case, $[Y_0', \tau_0]^{\mathrm{T}}$ is the initial assumption that can be set according to the center manifold of the equilibrium point. The elements in differential $D\varphi(x_n)$ can be derived from the state transition matrix $\Phi(t, t_0)$ and the dynamics $f(\mathbf{X})$ (see (66))

$$D\varphi(x_n) = \begin{bmatrix} \Phi(2,4) & f_2 \\ \Phi(3,4) & f_3 \end{bmatrix} \quad (74)$$

where the differential equation of $\Phi(t, t_0)$ is derived as

$$\dot{\Phi}(t, t_0) = \mathbf{A}(t)\Phi(t, t_0) \quad \mathbf{A}(t) = \frac{\partial f}{\partial \mathbf{X}} \quad (75)$$

with the initial value $\Phi(t_0, t_0) = \mathbf{I}_{4\times4}$. The terms of the Jacobian matrix $\mathbf{A}(t)$ are provided in Appendix A. The terms f_2 and f_3 are defined in (66).

When $\beta = 1$, the differential is

$$D_{\mathbf{X}_e}f = \begin{bmatrix} 0 & 0 & 1 & 0 \\ 0 & 0 & 0 & 1 \\ 9 & 0 & 0 & 5 \\ 0 & -3 & -5 & 0 \end{bmatrix} \quad (76)$$

Its eigenvalues and eigenvectors are computed as

$$\lambda = [\pm1.1525\ \pm4.5087i]^{\mathrm{T}} \quad (77)$$

$$\begin{cases} v_1 = [0.3936\ -0.5240\ \ 0.4536\ -0.6039]^{\mathrm{T}} \\ v_2 = [0.3936\ \ \ 0.5240\ -0.4536\ -0.6039]^{\mathrm{T}} \\ v_{3,4} = u_{3,4} \pm i w_{3,4} \end{cases} \quad (78)$$

where

$$\begin{cases} u_{3,4} = [0.1320\ 0\ 0\ -0.7740]^{\mathrm{T}} \\ w_{3,4} = [0\ 0.1717\ 0.5950\ 0]^{\mathrm{T}} \end{cases} \quad (79)$$

From the center manifold $u_{3,4}$ and the eigenvalues $\pm4.5087i$ in (77), the initial assumption that makes the value of the coordinate be -0.03 and its direction vector be
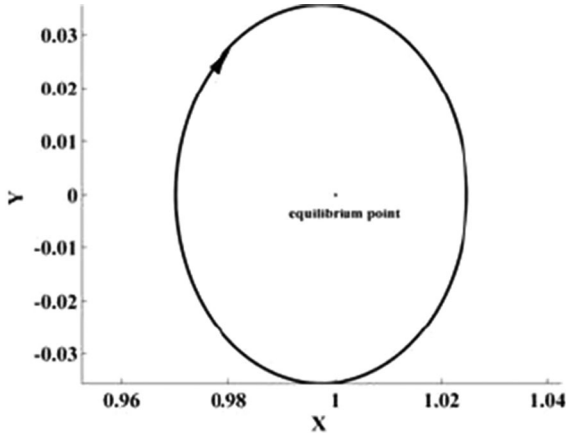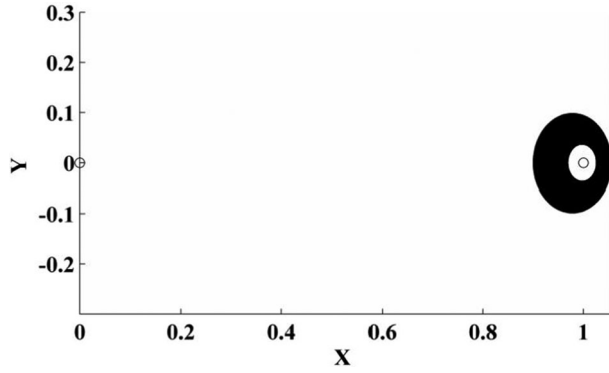
Fig. 23. View of the periodic orbit.

Fig. 24. Family of periodic orbits near the equilibrium point.

$u_{3,4}$ in the coordinates of the system is

$$\mathbf{X}_0 = \mathbf{X}_e + [-0.03 \quad 0 \quad 0 \quad 0.1759]^{\mathrm{T}} \tag{80}$$

$$\tau = T/2 = \pi/4.5087 = 0.6968 \tag{81}$$

where $\mathbf{X}_e = [1 \quad 0 \quad 0 \quad 0]^{\mathrm{T}}$ denotes the coordinates of the equilibrium point.

Coordinate X_0 is held fixed, and Y_0' and τ are searched for until the boundary conditions in (71) are satisfied. Then Newton iteration is applied and the initial conditions found are given as follows:

$$\mathbf{X}_0^* = [0.97 \quad 0 \quad 0 \quad 0.165855]^{\mathrm{T}} \tag{82}$$

$$T^* = 1.385182. \tag{83}$$

The periodic orbit is located near the equilibrium point and moves clockwise around it in Fig. 23. The computed method holds the X_0 coordinate fixed and adjusts the initial Y_0' and τ. Subsequently, a few different periodic orbits can be produced if the X_0 coordinates are changed, which comprise the family of this periodic orbit. Equations (82) and (83) are used as the starting place to move along the X-axis between $(x_e - 0.1)$ and $(x_e - 0.03)$ and parameter $\beta = 1$ remains unchanged, where $x_e = 1$ is the x coordinate of the equilibrium point. The family of computed orbits is shown in Fig. 24.
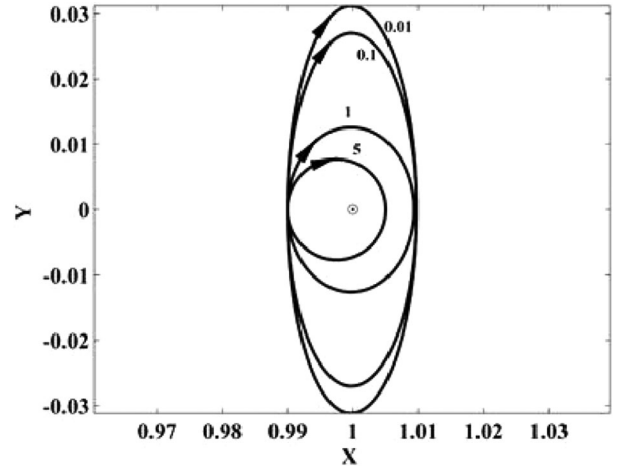

Fig. 25. Four periodic orbits with $\beta = 5, 1, 0.1,$ and 0.01.

C. Periodic Orbits at Different β values

A variable parameter β exists in (66) and the shape of the periodic orbit may differ if β is changed. We then compute the periodic orbits near the equilibrium point at different β values. First, let the value of β be 5, 1, 0.1, or 0.01, which are all positive. The initial assumptions are obtained using the same approach presented in Section V-B. Fig. 25 shows four orbits with different shapes and sizes.

The Y-axis velocities and the periods for the four periodic orbits in Fig. 25 are

$$[Y_0' \ T]_{\beta=5} = [0.131283 \quad 0.370903] \tag{84}$$

$$[Y_0' \ T]_{\beta=1} = [0.057360 \quad 1.392538] \tag{85}$$

$$[Y_0' \ T]_{\beta=0.1} = [0.059748 \quad 2.852129] \tag{86}$$

$$[Y_0' \ T]_{\beta=0.01} = [0.065168 \quad 3.015937]. \tag{87}$$

As shown in Fig. 25 and (84)−(87), the smaller β is, the larger the shape of the orbit and the longer the period. The Y-axis velocities are all positive, and the motion in the orbits is clockwise. After the numerical simulation, the shape of the computed orbits hardly changes when $0 < \beta < 0.01$, that is, the orbits are all similar to the orbit when $\beta = 0.01$. Essentially, when the absolute value $|\beta|$ is small, e.g., $|\beta| \leq 0.01$, parameter β no longer influences the shape of the periodic orbits.

For the condition $\beta < 0$, the periodic orbits have two modes, i.e., one mode is clockwise and the other is anti-clockwise. If the absolute value $|\beta|$ is small ($\beta < -0.01$), then the right side of (48) is dominated by the position states and the orbits are always moving clockwise (this conclusion will be proved by the following derivations of (107)). If the absolute value $|\beta|$ is larger, then the velocity states can affect the motion. Hence, the intersatellite Lorentz force acceleration on the right side of (48) is

$$\mathbf{F}_L = -\frac{3\beta}{|\mathbf{R}|^3}[-Y' \ X']^{\mathrm{T}} - \frac{3}{|\mathbf{R}|^3}[X \ Y]^{\mathrm{T}}. \tag{88}$$

The first term in (88) is evidently normal to the velocity. If the deputy satellite moves clockwise around the equilibrium point and parameter $\beta < 0$, then the first term
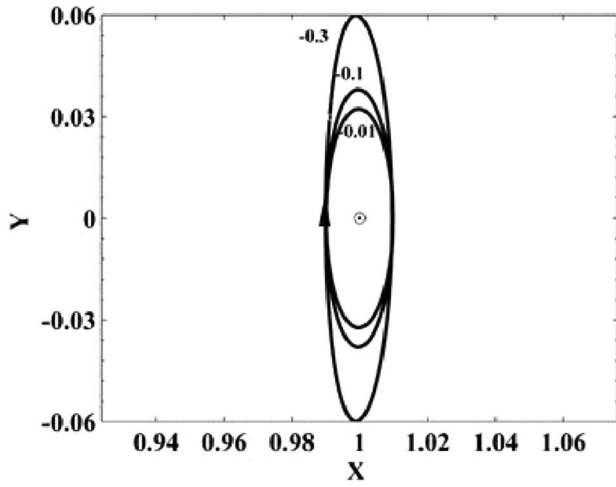
Fig. 26. Three periodic orbits with $\beta = -0.01, -0.1$, and -0.3.
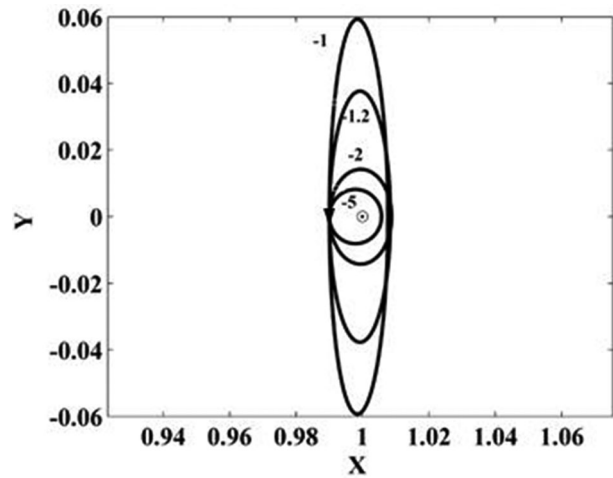

Fig. 27. Four periodic orbits with $\beta = -5, -2, -1.2$, and -1.

points outward to the path curve, thereby indicating a centrifugal force that will break the closed orbit. Therefore, the orbits found typically move counterclockwise. When $\beta = -0.01, -0.1$, and -0.3, in which the absolute values are small, the Y-axis velocities and the periods for the three orbits in Fig. 26 are

$$[Y'_0 \ T]_{\beta=-0.01} = [0.066652 \quad 3.050369] \tag{89}$$

$$[Y'_0 \ T]_{\beta=-0.1} = [0.074948 \quad 3.194880] \tag{90}$$

$$[Y'_0 \ T]_{\beta=-0.3} = [0.109457 \quad 3.446477]. \tag{91}$$

Evidently, all the orbits in Fig. 26 move clockwise. Thereafter, the counterclockwise orbits are computed when $|\beta|$ is large. Let $\beta = -5, -2, -1.2$, and -1. Then, the Y-axis velocities and the periods for the orbits are

$$[Y'_0 \ T]_{\beta=-5} = [-0.106523 \quad 0.488107] \tag{92}$$

$$[Y'_0 \ T]_{\beta=-2} = [-0.050934 \quad 1.792390] \tag{93}$$

$$[Y'_0 \ T]_{\beta=-1.2} = [-0.074084 \quad 3.239621] \tag{94}$$

$$[Y'_0 \ T]_{\beta=-1} = [-0.108209 \quad 3.474706]. \tag{95}$$

All the periodic orbits shown in Fig. 27 move counterclockwise, and their shapes and periods vary with β. The

numerical simulation results show that parameter β does not only affect the shape and period of periodic orbits, but also the moving direction.

D. Analytic Approximation of Periodic Orbits Using the Lindstedt–Poincare Method

When the planar dynamical equation, i.e., (48), is considered, the rotation angular rate ω_c of the dipole is assumed to be considerably larger than the mean orbital rate. Then, the approximation $\beta = 0$ when $|\beta| \le 0.01$) is obtained, and (48) can be written as

$$\begin{cases} X'' - 2Y' - 3X = -3\dfrac{X}{R^3} \\[2mm] Y'' + 2X' = -3\dfrac{Y}{R^3} \end{cases}. \tag{96}$$

The selection of a coordinate system that is centered at the equilibrium point is logical to focus on the motion near the equilibrium point $\mathbf{e}_1 = [1, 0]^{\mathrm{T}}$. Set $\boldsymbol{\rho} = [\rho_x, \rho_y]^{\mathrm{T}}$ and let $\boldsymbol{\rho} = \mathbf{R} - \mathbf{e}_1$. Then, (96) can be transformed into

$$\begin{cases} \rho_x'' - 2\rho_y' - 3(\rho_x + 1) = \dfrac{\partial \Omega}{\partial \rho_x} \\[3mm] \rho_y'' + 2\rho_x' = \dfrac{\partial \Omega}{\partial \rho_y} \end{cases} \tag{97}$$

where

$$\Omega = \frac{3}{|\mathbf{R}|} = \frac{3}{|\boldsymbol{\rho} + \mathbf{e}_1|} = 3 \cdot \sum_{n=0}^{\infty} p_n(-\rho_x/|\boldsymbol{\rho}|)|\boldsymbol{\rho}|^n$$

$$= 3 - 3\rho_x + U \tag{98}$$

$$U = 3 \cdot \sum_{n=2}^{\infty} p_n(-\rho_x/|\boldsymbol{\rho}|)|\boldsymbol{\rho}|^n$$

$$= \sum_{n=2}^{\infty} c_n p_n(\rho_x/|\boldsymbol{\rho}|)|\boldsymbol{\rho}|^n \tag{99}$$

$$c_n = (-1)^n \cdot 3 \tag{100}$$

where p_n denotes the Legendre polynomials. The linear approximation to the equations of motion is achieved by considering only the first term ($n = 2$) in U, i.e.,

$$\begin{cases} \rho_x'' - 2\rho_y' - 9\rho_x = 0 \\ \rho_y'' + 2\rho_x' + 3\rho_y = 0 \end{cases} \tag{101}$$

which is a set of linear ordinary differential equations. Its characteristic polynomial is

$$\lambda^4 - 2\lambda^2 - 27 = 0 \tag{102}$$

where λ is computed as

$$\lambda_{1,2} = \pm\sqrt{2\sqrt{7}+1}, \quad \lambda_{3,4} = \pm i\sqrt{2\sqrt{7}-1}. \tag{103}$$

Therefore, the solution for the linear equations in (101) can be written as follows:

$$\begin{cases} \rho_x(\tau) = A_1 e^{\upsilon\tau} + A_2 e^{-\upsilon\tau} + A_3 \cos\lambda\tau + A_4 \sin\lambda\tau \\ \rho_y(\tau) = -k_1 A_1 e^{\upsilon\tau} + k_1 A_2 e^{-\upsilon\tau} \\ \qquad\qquad - k_2 A_3 \cos\lambda\tau + k_2 A_4 \sin\lambda\tau \end{cases}$$
(104)

where

$$\upsilon = \sqrt{2\sqrt{7}+1}, \qquad \lambda = \sqrt{2\sqrt{7}-1} \quad (105)$$

$$k_1 = \frac{1}{2}(9-\upsilon^2)/\upsilon, \quad k_2 = \frac{1}{2}(9+\lambda^2)/\lambda \quad (106)$$

and A_1, A_2, A_3, and A_4 are arbitrary constants determined using the initial conditions.

To obtain the periodic solutions for (104), set $A_1 = A_2 = 0$, which results in the following solution:

$$\begin{cases} \rho_x(\tau) = -A_x \cos(\lambda\tau + \phi) \\ \rho_y(\tau) = kA_x \sin(\lambda\tau + \phi) \end{cases}$$
(107)

where $k = k_2 \approx 3.2$. The solution for (107) is a periodic orbit that moves clockwise around the equilibrium point, which proves that the periodic orbits are always moving clockwise when the absolute value $|\beta|$ is sufficiently small.

The perturbation technique of Lindstedt $-$ Poincare is adopted to find better approximations to the solutions for motion near the equilibrium point when $|\beta|$ is sufficiently small. When $\xi = \omega\tau$ is allowed for a frequency correction, the form of perturbation analysis is assumed as

$$\begin{cases} \rho_x(\xi) = \varepsilon x_1(\xi) + \varepsilon^2 x_2(\xi) + \varepsilon^3 x_3(\xi) + ... \\ \rho_y(\xi) = \varepsilon y_1(\xi) + \varepsilon^2 y_2(\xi) + \varepsilon^3 y_3(\xi) + ... \end{cases}$$
(108)

and let

$$\omega = 1 + \varepsilon\omega_1 + \varepsilon^2\omega_1 + ... \quad . \quad (109)$$

When these quantities are substituted into the equations for motion in (97) and equating components of the same order, a third-order approximation for the periodic orbit is

$$\begin{cases} x(\xi) = \rho_{20} - A_x \cos\tau_1 + \rho_{21} \cos 2\tau_1 + \rho_{31} \cos 3\tau_1 \\ y(\xi) = (kA_x + \sigma_{32}) \sin\tau_1 + \sigma_{21} \sin 2\tau_1 + \sigma_{31} \sin 3\tau_1 \end{cases}$$
(110)

where the expressions for the coefficients $\rho_{20}, \rho_{21}, \rho_{31}, \sigma_{32}, \sigma_{21}, \sigma_{31}$ and τ_1 are provided in Appendix B.

The expression in (110) is the approximate solution for the planar periodic orbit with $\beta \approx 0$, which can provide an accurate prediction for the periodic orbit near the equilibrium point if β is small.

To verify the approximate solution, let $A_x = 0.01$. Then, the initial states and the orbital period computed using (110) are

$$[X_0 \ Y_0 \ X_0' \ Y_0']^T = [-0.010075 \ 0 \ 0 \ 0.066599]^T \quad (111)$$
$$T = 3.033579. \quad (112)$$

After setting $\beta = 0.005, 0.01$, and 0.05, the Newton method is used and the initial conditions are numerically
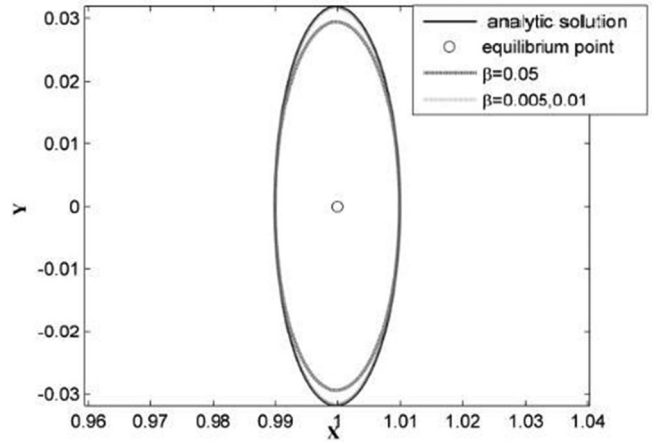

Fig. 28. Comparison of the analytic solution and the numerical solution.

computed

$$[X_0 \ Y_0 \ X_0' \ Y_0']^T_{\beta=0.005} = [-0.010075 \ 0 \ 0 \ 0.066015]^T$$
(113)
$$T_{\beta=0.005} = 3.024622 \quad (114)$$
$$[X_0 \ Y_0 \ X_0' \ Y_0']^T_{\beta=0.01} = [-0.010075 \ 0 \ 0 \ 0.065652]^T$$
(115)
$$T_{\beta=0.01} = 3.015941 \quad (116)$$
$$[X_0 \ Y_0 \ X_0' \ Y_0']^T_{\beta=0.05} = [-0.010075 \ 0 \ 0 \ 0.062987]^T$$
(117)
$$T_{\beta=0.05} = 2.944815. \quad (118)$$

When (111), (112), and (113)$-$(118) are considered, the initial conditions, i.e., (111) and (112), obtained using the analytic solution are found to be relatively similar to the initial conditions, i.e., (113)$-$(116), numerically computed using the Newton method when $\beta = 0.005$ and 0.01. The difference between the periods is a time unit margin of less than 0.02. In the case of $\beta = 0.05$, the differences between the analytic solutions, i.e., (111) and (112), and the numerical solutions, i.e., (117) and (118), increase. The orbits obtained using the two methods are shown in Fig. 28, in which the two orbits for $\beta = 0.005$ and $\beta = 0.01$ are overlapping. In conclusion, the analytical solutions are appropriate and reasonable when β is sufficiently small.

In this section, the planar periodic orbits near the equilibrium points are numerically computed via differential correction, and the special case when $|\beta| \leq 0.01$ is analytically solved using the Lindstedt$-$Poincare method. The unstable periodic orbits near the equilibrium points indicate that the deputy satellite located near the equilibrium point can travel through the point. In addition, the analytical solution for the case when $|\beta| \leq 0.01$ can provide a reference orbit for the deputy satellite being maintained.

VI. CONCLUDING REMARKS AND PROSPECTS

A dynamical system of space relative motion that involves intersatellite Lorentz force was established based on the assumptions that a chief satellite would be capable of

generating a rotating magnetic dipole, while a constantly charged deputy satellite was moving close to the magnetic field of the chief satellite. Subsequently, dynamical systems theory was applied to analyze the system, including deriving equilibrium points and their stabilities, finding an integral constant, and depicting zero-velocity surfaces. The existence of bounded periodic relative orbits was discovered using Poincare maps with respect to zero-velocity surfaces. The periodic orbits around the equilibrium points were found and analyzed at different β values (particularly when β was sufficiently small, analytic solutions were obtained via the Lindstedt−Poincare method) using differential corrections methods. Meanwhile, the orbits of the chief satellite and the deputy satellite could be deduced through the relative orbit. However, the dynamics of the proposed relative motion is insufficient to provide complete understanding. It is also more complicated than originally envisioned.

This study shows that formation in the presence of intersatellite Lorentz force is possible with the appropriate selection of initial relative states. If the parameters $((q/m)$, B_0, ω_c, ϵ, and $n)$ are set rationally (as presented in Section III-B), the range between the chief satellite and the equilibrium point is approximately 2.3 m. Therefore, implementing formation at the meters scale is feasible. However, the problem of establishing a desired charge or magnetic dipole moment in space, particularly a substantial amount of charge and magnetic strength, must be resolved. Additional details regarding the aforementioned technologies are presented in [28] and [29].

New types of formation flying scenarios can be envisioned based on the understanding of bounded periodic orbits near the chief satellite and the equilibrium points. For example, a space station can maintain a number of small service satellites using propellantless Lorentz force. Another possible application is the implementation of non-contact capture of charged space debris using spacecraft via Lorentz force and towing them to desired orbits. The charged debris can be captured through the periodic orbits around the equilibrium points and placed into bounded periodic orbits in which debris will be unable to escape.

APPENDIX

A. Terms of the Derivative of $\mathbf{f}(\mathbf{X})$ Evaluated at the Point $\mathbf{X}_e (q/m < 0)$

$$\frac{\partial f_1}{\partial X} = \frac{\partial f_1}{\partial Y} = \frac{\partial f_1}{\partial Z} = \frac{\partial f_1}{\partial Y'} = \frac{\partial f_1}{\partial Z'} = 0 \qquad \frac{\partial f_1}{\partial X'} = 1 \tag{119}$$

$$\frac{\partial f_2}{\partial X} = \frac{\partial f_2}{\partial Y} = \frac{\partial f_2}{\partial Z} = \frac{\partial f_2}{\partial X'} = \frac{\partial f_2}{\partial Z'} = 0 \qquad \frac{\partial f_2}{\partial Y'} = 1 \tag{120}$$

$$\frac{\partial f_3}{\partial X} = \frac{\partial f_3}{\partial Y} = \frac{\partial f_3}{\partial Z} = \frac{\partial f_3}{\partial X'} = \frac{\partial f_3}{\partial Y'} = 0 \qquad \frac{\partial f_3}{\partial Z'} = 1 \tag{121}$$

$$\frac{\partial f_4}{\partial X} = 3 - 3\frac{3X^2 + Y^2 - 2Z^2 - 2\beta XY'}{R^5} + 15\frac{X[\beta Y'(-X^2 - Y^2 + 2Z^2) - 3\beta YZZ' + X(X^2 + Y^2 - 2Z^2)]}{R^7} \tag{122}$$

$$\frac{\partial f_4}{\partial Y} = -3\frac{2XY - 3\beta ZZ' - 2\beta YY'}{R^5} + m15\frac{Y[\beta Y'(-X^2 - Y^2 + 2Z^2) - 3\beta YZZ' + X(X^2 + Y^2 - 2Z^2)]}{R^7} \tag{123}$$

$$\frac{\partial f_4}{\partial Z} = -3\frac{4\beta ZY' - 3\beta YZ' - 4XZ}{R^5} + 15\frac{Z[\beta Y'(-X^2 - Y^2 + 2Z^2) - 3\beta YZZ' + X(X^2 + Y^2 - 2Z^2)]}{R^7} \tag{124}$$

$$\frac{\partial f_4}{\partial X'} = 0 \tag{125}$$

$$\frac{\partial f_4}{\partial Y'} = 2 - 3\frac{\beta(-X^2 - Y^2 + 2Z^2)}{R^5} \tag{126}$$

$$\frac{\partial f_4}{\partial Z'} = 9\frac{\beta YZ}{R^5} \tag{127}$$

$$\frac{\partial f_5}{\partial X} = -3\frac{2XY + 3\beta ZZ' + 2\beta XX'}{R^5} + 15\frac{X[\beta X'(X^2 + Y^2 - 2Z^2) + 3\beta XZZ' + Y(X^2 + Y^2 - 2Z^2)]}{R^7} \tag{128}$$

$$\frac{\partial f_5}{\partial Y} = -3\frac{X^2 + 3Y^2 - 2Z^2 + 2\beta YX'}{R^5} + 15\frac{Y[\beta X'(X^2 + Y^2 - 2Z^2) + 3\beta XZZ' + Y(X^2 + Y^2 - 2Z^2)]}{R^7} \tag{129}$$

$$\frac{\partial f_5}{\partial Z} = -3\frac{3\beta XZ' - 4\beta ZX' - 4YZ}{R^5} + 15\frac{Z[\beta X'(X^2 + Y^2 - 2Z^2) + 3\beta XZZ' + Y(X^2 + Y^2 - 2Z^2)]}{R^7} \tag{130}$$

$$\frac{\partial f_5}{\partial X'} = -2 - 3\frac{\beta(X^2 + Y^2 - 2Z^2)}{R^5} \tag{131}$$

$$\frac{\partial f_5}{\partial Y'} = 0 \tag{132}$$

$$\frac{\partial f_5}{\partial Z'} = -9\frac{\beta XZ}{R^5} \tag{133}$$

$$\frac{\partial f_6}{\partial X} = -9\frac{Z(2X - \beta Y')}{R^5} - 45\frac{XZ(\beta YX' - \beta XY' + X^2 + Y^2)}{R^7} \tag{134}$$

$$\frac{\partial f_6}{\partial Y} = -9\frac{Z(2Y + \beta X')}{R^5} - 45\frac{YZ(\beta YX' - \beta XY' + X^2 + Y^2)}{R^7} \tag{135}$$

$$\frac{\partial f_6}{\partial Z} = -1 - 9\frac{\beta YX' - \beta XY' + X^2 + Y^2}{R^5} \tag{136}$$

$$-45\frac{Z^2(\beta YX' - \beta XY' + X^2 + Y^2)}{R^7}$$

$$\frac{\partial f_6}{\partial X'} = -9\frac{\beta YZ}{R^5} \tag{137}$$

$$\frac{\partial f_6}{\partial Y'} = 9\frac{\beta XZ}{R^5} \tag{138}$$

$$\frac{\partial f_6}{\partial Z'} = 0 \tag{139}$$

B. Expressions for the Coefficients in (110)

$$\sigma_{32} = -\frac{k}{2\lambda}\beta_6 \tag{140}$$

$$\sigma_{31} = \frac{6\lambda\gamma_3 - \beta_3(9\lambda^2 + 9)}{81\lambda^4 + 18\lambda^2 - 27} \tag{141}$$

$$\sigma_{21} = \frac{4\lambda\gamma_1 - \beta_1(4\lambda^2 + 9)}{16\lambda^4 + 8\lambda^2 - 27} \tag{142}$$

$$\rho_{20} = -\frac{1}{9}\alpha_1 \tag{143}$$

$$\rho_{21} = \frac{4\lambda\beta_1 - \gamma_1(4\lambda^2 - 3)}{16\lambda^4 + 8\lambda^2 - 27} \tag{144}$$

$$\rho_{31} = \frac{6\lambda\beta_3 - \gamma_3(9\lambda^2 - 3)}{81\lambda^4 + 18\lambda^2 - 27} \tag{145}$$

$$\tau_1 = \lambda\xi + \phi \tag{146}$$

$$k = \frac{1}{2}(9 + \lambda^2)/\lambda \tag{147}$$

$$\lambda = \sqrt{2\sqrt{7} - 1} \tag{148}$$

$$\beta_1 = \frac{3}{2}c_3 k A_x^2 \tag{149}$$

$$\beta_3 = \frac{3}{2}c_3 A_x(\sigma_{21} - k\rho_{21}) - \frac{3}{8}kc_4 A_x^3(k^2 + 4) \tag{150}$$

$$\beta_6 = \nu_2 + 2\omega_2\lambda A_x(\lambda k - 1) \tag{151}$$

$$\gamma_1 = \frac{3}{2}c_3 A_x^2\left(1 + \frac{k^2}{2}\right) \tag{152}$$

$$\gamma_3 = -\frac{3}{2}c_3 A_x(2\rho_{21} - k\sigma_{21}) - \frac{1}{2}c_4 A_x^3(k^2 + 2) \tag{153}$$

$$\nu_1 = -3c_3 A_x\left(2\rho_{20} + \rho_{21} + \frac{k}{2}\sigma_{21}\right) + \frac{3}{2}c_3 A_x^3(k^2 - 2) \tag{154}$$

$$\nu_2 = \frac{3}{2}c_3 A_x(\sigma_{21} - 2k\rho_{20} + k\rho_{21}) + \frac{3}{2}c_4 k A_x^3\left(\frac{3}{4}k^2 - 1\right) \tag{155}$$

$$\alpha_1 = \frac{3}{2}c_3 A_x^2\left(1 - \frac{k^2}{2}\right) \tag{156}$$

$$\omega_2 = \frac{\nu_1 - k\nu_2}{2A_x\lambda[\lambda(k^2 + 1) - 2k]} \tag{157}$$

REFERENCES

[1] M. A. Peck
Lorentz-actuated orbits: Electrodynamic propulsion without a tether
NASA Inst. Adv. Concepts, Washington, DC, USA, *Phase I Final Report*, May 2006.

[2] L. Schaffer and J. A. Burns
The dynamics of weakly charged dust: Motion through Jupiter's gravitational and magnetic fields
J. Geophys. Res., vol. 92, no. A3, pp. 2264–2280, Mar. 1987.

[3] M. E. Hough
Lorentz force perturbations of a charged ballistic missile
In *Proc. AIAA Guid. Control Conf.*, Aug. 9–11, 1982, AIAA: 1982–1549.

[4] D. Vokrouhlicky
The geomagnetic effects on the motion of electrically charged artificial satellite
Celest. Mech. Dyn. Astron., vol. 46, no. 1, pp. 85–104, 1989.

[5] Y. Abdel-Aziz
Lorentz force effects on the orbit of a charged artificial satellite: A newapproach
Appl. Math. Sci., vol. 1, no. 31, pp. 1511–1518, 2007.

[6] S. T. Lai
An overview of electron and ION beam effects in charging and discharging of spacecraft
IEEE Trans. Nucl. Sci.. vol. 36, no. 6, pp. 2027–2032, Dec. 1989.

[7] K. Torkar *et al.*
Active spacecraft potential control for cluster implementation and first results
Ann. Geophys., vol. 19, pp. 1289–1302, 2001.

[8] B. Streetman and M. A. Peck
New synchronous orbits using the geomagnetic lorentz force
J. Guid., Control Dynam., vol. 30, no. 6, pp. 1677–1690, 2007.

[9] B. Streetman and M. A. Peck
A general bang-bang control method for lorentz augmented orbits
In *Proc. AAS Spaceflight Mech. Meeting*, Jan. 27–31, 2008, AAS: 8–111.

[10] B. Streetman and A. Peck
Gravity-assist maneuvers augmented by the lorentz force
J. Guid., Control Dynam., vol. 32, no. 5, pp. 1639–1647, 2009.

[11] J. A. Atchison, B. Streetman, and M. A. Peck
Prospects for lorentz augmentation in jovian captures
In *Proc. AIAA Guid., Navig. Control Conf. Exhib.*, Keystone, CO, USA, Aug. 21–24, 2006, AIAA: 2006–6596.

[12] G. E. Pollock, J. W. Gangestad, and J. M. Longuski
Responsive coverage using propellantless satellites
In *Proc. AIAA/6th Responsive Space Conf.*, Los Angeles, CA, USA, Apr. 28–May 1, 2008, AIAA-RS6-2008–2002.

[13] G. E. Pollock, J. W. Gangestad, J. M. Longuski
Inclination change in low-earth orbit via the geomagnetic lorentz force
J. Guid., Control Dynam., vol. 33, no. 5, pp. 1387–1395, 2010.

[14] J. W. Gangestad, G. E. Pollock, and J. M. Longuski
Lagrange's planetary equations for the motion of electrostatically charged spacecraft
Celest. Mech. Dynam. Astron., vol. 108, no. 2, pp. 125–145, 2010.

[15] E. Kong, D. Kwon, S. Schweighart, L. Elias, R. Sedwick, and D. Miller
Electromagnetic formation flight for multi-satellite arrays
J. Spacecraft Rockets, vol. 41, no. 4, pp. 659–666, 2004.

[16] U. Ahsun and D. W. Miller
Dynamics and control of electromagnetic satellite formations
In *Proc. Amer. Control Conf.*, 2006, pp. 1–6, doi: 10.1109/ACC. 2006.1656469.

[17] A. Umair, D. W. Miller, J. L. Ramirez

Control of electromagnetic satellite formations in near-earth orbit
J. Guid., Control Dynam., vol. 33, no. 6, pp. 1883–1891, 2010.

[18] L. B. King, G. G. Parker, S. Deshmukh, and J. H. Chong
Study of interspacecraft coulomb forces and implications for formation flying
J. Propulsion Power, vol. 19, no. 3, pp. 497–505, 2003.

[19] H. Schaub
Stabilization of satellite motion relative to a coulomb spacecraft formation
J. Guid., Control Dynam., vol. 28, no. 6, pp. 1231–1239, 2005.

[20] S. Wang and H. Schaub
One-dimensional constrained coulomb structure control with charge saturation
IEEE Trans. Aerosp. Electron. Syst., vol. 48, no. 1, pp. 3–15, Jan. 2012.

[21] L. Felicetti and G. B. Palmerini
Evaluation of control strategies for spacecraft electrostatic formation keeping
In *Proc. IEEE Aerosp. Conf.*, 2014, doi: 10.1109/AERO.2014.6836452.

[22] M. A. Peck, B. Streetman, C. M. Saaj, and V. Lappas
Spacecraft formation flying using lorentz forces
J. Brit. Interplanet. Soc., vol. 60, no. 7, pp. 263–267, 2007.

[23] G. E. Pollock, J. W. Gangestad, and J. M. Longuski
Analysis of lorentz spacecraft motion about earth using the Hill-Clohessy-Wiltshire equations
In *Proc. AIAA/AAS Astrodyn. Spec. Conf. Exhib.*, Honolulu, HI, USA, Aug. 18–21, 2008, AIAA: 2008–6762.

[24] C. Peng and Y. Gao
Lorentz-force-perturbed orbits with application to j2-invariant formation
Acta Astronaut., vol. 44, no, 5, pp. 12–28, 2012.

[25] C. Peng and Y. Gao
Near-circular low-earth-orbit spacecraft formation control with lorentz force
Chin. J. Theor. Appl. Mech., vol. 44, no. 5, pp. 851–860, 2012. (in Chinese).

[26] L. A. Sobiesiak and C. J. Damaren
Lorentz-augmented spacecraft formation reconfiguration
IEEE Trans. Control Syst. Technol., vol. 24, no. 2, pp. 514–524, Mar. 2016.

[27] W. S. Koon
Dynamical systems, the three-body problem, and space mission design
In *Proc. Int. Conf. Differ. Equ.*, Berlin, Germany, 1999, pp. 1167–1181.

[28] M. A. Peck
Prospects and challenges for lorentz-augmented orbits
In *Proc. AIAA Guid., Navig., Control Conf. Exhib.*, San Francisco, CA, USA, Aug. 15–18, 2005, AIAA: 2005–5995.

[29] D. W. Kwon and D. W. Miller
Electromagnetic formation flight of satellite arrays
M.S. thesis, Dept. Aeronaut. Astronaut., Massachusetts Inst. Technol., Cambridge, MA, USA, Feb. 2005.

[30] H. Schaub and J. L. Junkins
Analytical Mechanics of Space Systems. Reston, VA, USA: AIAA, 2003.

[31] J. D. Jackson
Classical Electrodynamics, 3rd ed. Hoboken, NJ, USA: Wiley, 1999.

[32] T. Alfriend, S. Vadali, P. Gurfil, J. How, and L. Breger
Spacecraft Formation Flying
New York, NY, USA: Elsevier, 2010.

[33] J. D. James
Symmetric periodic orbits of the circular restricted three body problem and their stable and unstable manifolds
Celest. Mech. Notes Set 5, Dec. 22, 2006.

Chao Peng received the B.S. degree in mechanical engineering from the Taiyuan University of Technology, China, in 2008 and the M.S. degree in dynamics and control from the Chinese Academy of Sciences, Beijing, China, in 2012.

Since 2012, he has been a Junior Engineer with the Technology and Engineering Center of Space Utilization, Chinese Academy of Sciences. His academic interest includes spacecraft dynamics and control, trajectory optimization, and space mission design.

Yang Gao received the B.S. degree in automatic control from the Beijing University of Aeronautics and Astronautics in 1997, the M.S. degree in remote sensing from the Chinese Academy of Sciences, Beijing, China, in 2000, and the Doctoral degree in dynamics and control from the University of Missouri-Columbia, USA, in 2003.

From 2004 to 2005, he was a Postdoctoral Research Fellow at the University of Missouri-Columbia. Since 2005, he has been an Associate Research Fellow at the Academy of Opto-Electronics, Chinese Academy of Sciences, Beijing. He is currently a Research Professor at the Technology and Engineering Center of Space Utilization, Chinese Academy of Sciences. His academic interests include orbit determination, spacecraft dynamics and control, guidance and navigation, trajectory optimization, and space mission design.